COMPARISON OF AN AXISYMMETRIC AND A PLANAR SHOCK TUNNEL NOZZLE

A Thesis

by

MCKENNA L. ROBERTS

Submitted to the Graduate and Professional School
Texas A&M University
in partial fulfillment of the requirements for the degree of

MASTER OF SCIENCE

Chair of Committee,	Rodney D. W. Bowersox
Committee Members,	Edward White
	Waruna Kulatilaka
Head of Department,	Srinivas Vadali

August 2021

Major Subject: Aerospace Engineering

ABSTRACT

In order to expand the capabilities of Texas A&M Universitys Hypervelocity Expansion Tunnel to include a reflected shock tunnel mode of operation, a comparison study between axisymmetric and planar nozzles at varying Mach numbers was conducted. The nozzle curves were developed using method of characteristics codes that include viscous effects. Computational fluid dynamics simulations were conducted using ANSYS Fluent to validate these curves. Preliminary mechanical designs for both a variable Mach number planar nozzle and a Mach 8 axisymmetric nozzle were created using the computer aided design software Solidworks. From these results and gathered knowledge, comparisons between the two types of nozzles were performed, leading to a recommendation of which type would be best suited for both external aerodynamics and internal propulsion studies.

CONTRIBUTORS AND FUNDING SOURCES

Contributors

This work was supported by a thesis committee consisting of Dr. Rodney D. W. Bowersox and Dr. Edward White of the Department of Aerospace Engineering and Dr. Waruna Kulatilaka of the Department of Mechanical Engineering.

All work conducted for the thesis was completed by the student independently unless otherwise stated.

Funding Sources

Graduate study was supported by the Office of the Undersecretary of Defense Research and Engineering (OUSD(R+E)) Vannevar Bush Faculty Fellowship (Grant No. N00014-18-3020).

NOMENCLATURE

Acronyms and Abbreviations

ACE	Actively Controlled Expansion
BL	Boundary Layer
CAD	Computer Aided Design
CFD	Computational Fluid Dynamics
HST	Hypervelocity Shock Tunnel
HXT	Hypervelocity Expansion Tunnel
MOC	Method of Characteristics
NAL	National Aerothermochemistry and Hypersonics Laboratory
TAMU	Texas A&M University

Variables

α	Thermal Diffusivity
k	Thermal Conductivity
Q	Heat Flux
T	Temperature
T_i	Initial Temperature
τ	Time
x	Distance

TABLE OF CONTENTS

LIST OF FIGURES

FIGURE Page

LIST OF TABLES

1. INTRODUCTION

1.1 Motivation

The Hypervelocity Expansion Tunnel (HXT) located at Texas A&M Universitys National Aerothermochemistry and Hypersonics Laboratory (NAL) is an expansion facility capable of reaching high enthalpy flows at a range of Mach numbers from 5 to 23 with very short run times on the order of 1 millisecond. Figure 1.1 below shows the current operating envelope of HXT along with the conditions that have been reached during actual runs. Figure 1.2 shows the computer aided design (CAD) of the facility in full, with the flow running from top to bottom. This tunnel uses a double diaphragm system of one steel primary diaphragm and one Mylar secondary diaphragm in conjuncture with a diverging nozzle to achieve the desired test conditions. The use of the secondary diaphragm causes complexities. However, this tunnel was designed to also act as a shock tunnel by moving the steel primary diaphragm to the secondary diaphragm location and using it as the one and only diaphragm (see Figure 1.4). Unfortunately, with the diverging nozzle, test times are not increased significantly [1] [2].

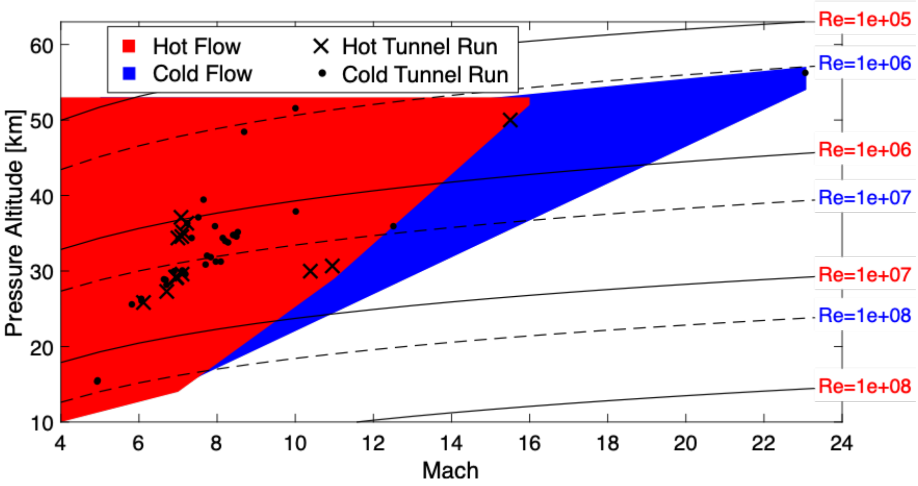

Figure 1.1: Operating envelope of the current HXT.

By using a converging-diverging nozzle in place of the diverging nozzle, HXT becomes a reflected shock tunnel, yielding the benefit of both removing the complexity caused by the secondary diaphragm and increasing test times. The purpose of this paper is to discuss the exploration into converging-diverging nozzle designs for the shock tunnel mode of HXT, known as the Hypervelocity Shock Tunnel (HST).

1.2 Background

1.2.1 Tunnel Types

1.2.1.1 Expansion Tunnels

Using Figure 1.2 as a guide, the different section of the expansion tunnel are explained in the following. An expansion tunnel is made of three sections which are separated by diaphragms. The first section is commonly called the driver and is separated from the next section by the primary diaphragm. This section typically holds high pressure gas, for HXT this is anywhere between 500 and 2000 psi. The next section is the test gas or driven section and is held at a much lower pressure than the driver, usually around or less than an atmosphere. This is separated from the third section, the acceleration or expansion section, by the secondary diaphragm. The acceleration section is at an even lower pressure than the driven, typically between one or one one thousandths of a Torr.

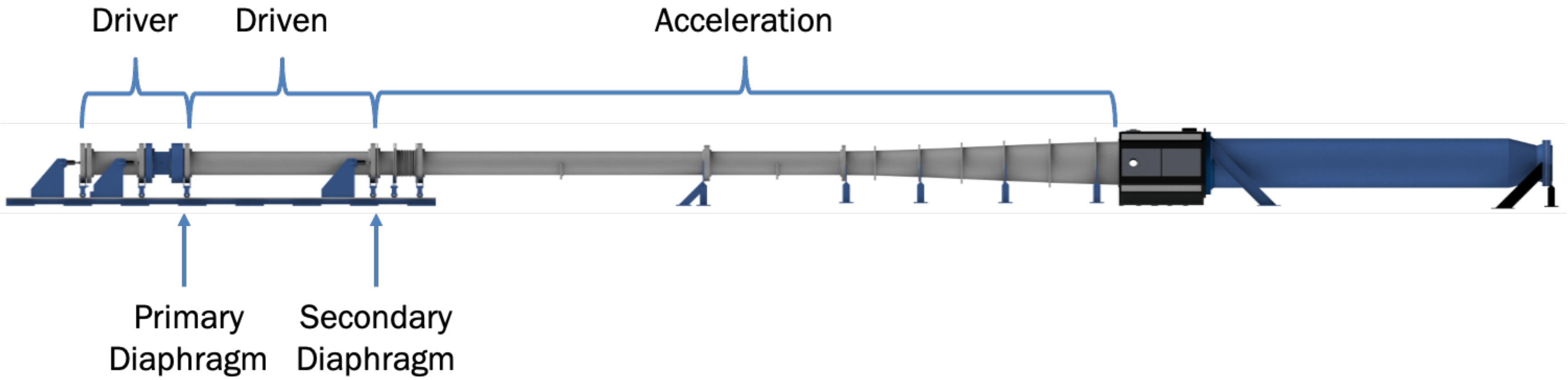

Figure 1.2: Current HXT facility configuration with parts labeled.

For HXT, the primary diaphragm is made of steel with an X scored at certain depths depending on the desired burst pressure. The second diaphragm is made of Mylar and theoretically breaks upon contact with the initial shock wave produced by the rupturing of the primary diaphragm. By setting the pressures and types of gas within each section, a variety of flight conditions can be created [3].

Upon the rupture of the primary diaphragm, a shock wave is produced and shock heats the air in the test gas section before rupturing the secondary diaphragm. When this happens, another shock wave is produced and moves forward into the acceleration section while an expansion wave passes back through the shock heated test gas, causing the flow to accelerate [3] [4]. This flow is further expanded and accelerated by the diverging nozzle into the test section. As was mentioned before, expansion tunnels have significantly short test times on the order of a few milliseconds [3]. An example x-t diagram for HXT is shown below for Mach 7.65, which is on the slower end for HXT. The expansion waves are represented as blue lines, the contact surfaces as black dashed lines, and the shock wave as the red dotted line. The origins of these waves are the diaphragms breaking, with the primary diaphragm at a distance, x, and time, t, value of 0. The test time is located at the x value of 65 as the time between the contact surface and the first expansion wave. This diagram was produced by a MATLAB code that was developed by a past graduate student, Gabe Aguilar.

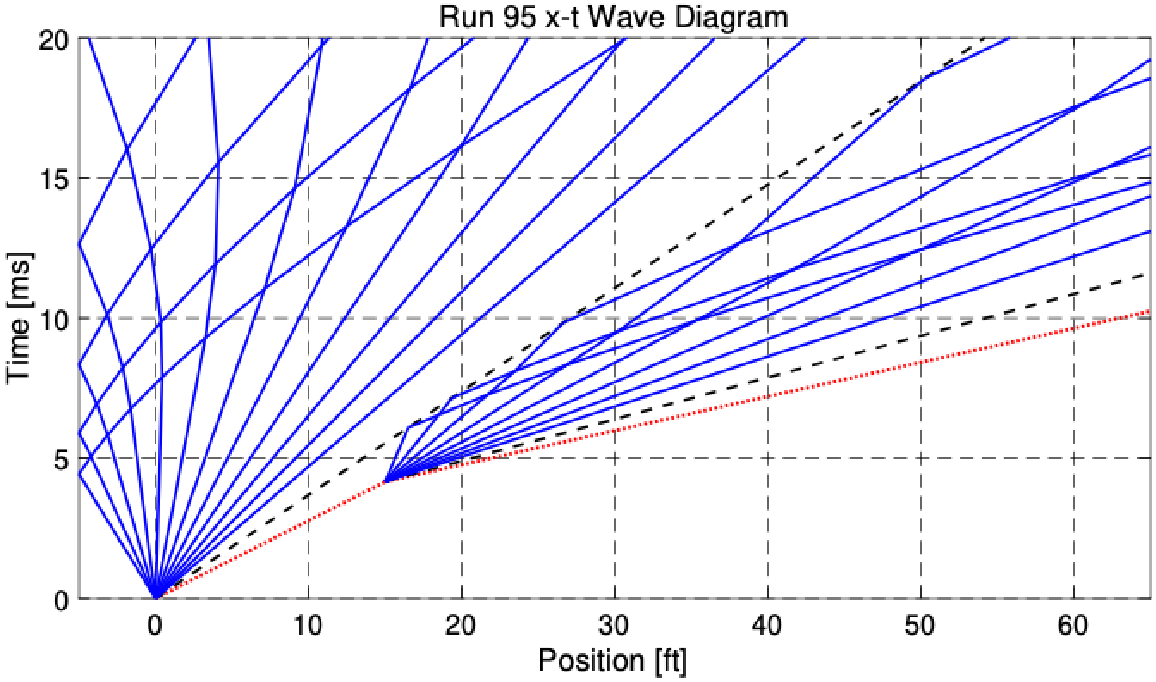

Figure 1.3: x-t diagram for HXT at Mach 7.65.

1.2.1.2 Shock Tunnels

Shock tubes and tunnels work much like the expansion tunnel except they employ the use of only one diaphragm which removes the complexities posed by the secondary diaphragm. The major difference between the tube and tunnel is the addition of a nozzle to the end of the acceleration section. Furthermore, a shock tunnel can be divided into reflected-shock and non-reflected-shock type. A shock tube has a Mach number limit of about 3 and is incapable of producing hypersonic flow. But with the addition of a nozzle, the shock tunnel can achieve higher Mach numbers [1]. Without changing the current expansion nozzle but allowing for only one diaphragm turns HXT into a non-reflected-shock tunnel, seen in Figure 1.4.

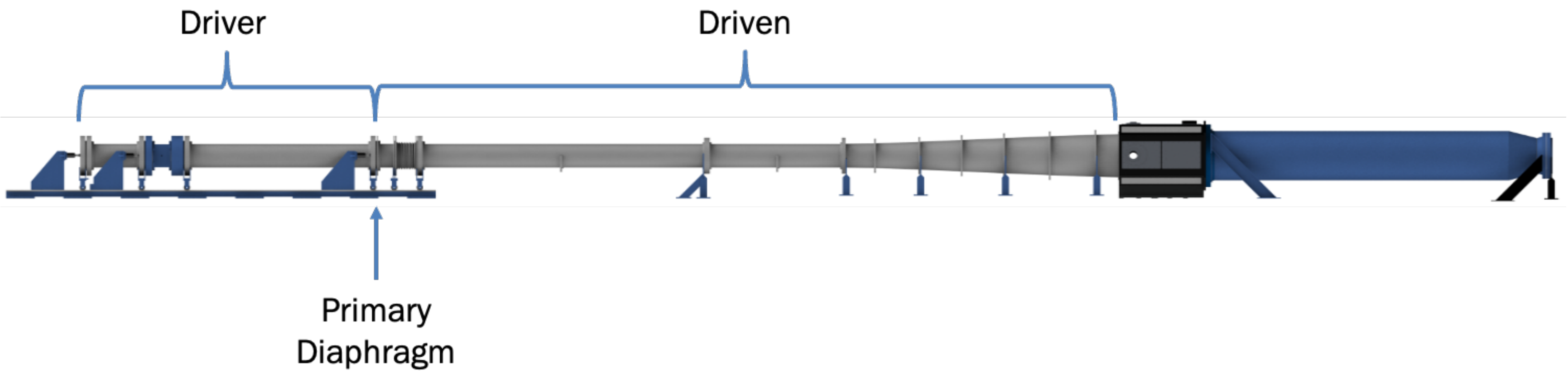

Figure 1.4: Non-reflected shock tunnel configuration of HXT with parts labeled.

In non-reflected shock tunnel mode, the test times are also significantly short, remaining near 1 millisecond [2]. A typical x-t diagram for a non-reflected shock tube is shown in Figure 1.5 from Martin [1]. The s vector is the shock wave, the c vector as the contact surface, and the R vector as the expansion waves. The test time is between the shock wave and the contact surface at the test section location, which for non-reflection shock tunnels is located before the shock wave reflects. To maximize the testing time, the length of the tube is increased to delay interaction between the reflection of the waves and the contact surface [1]. In addition to the increasing the lengths of the sections, creating a stronger shock wave and using other types of gases can increase test time as well [1].

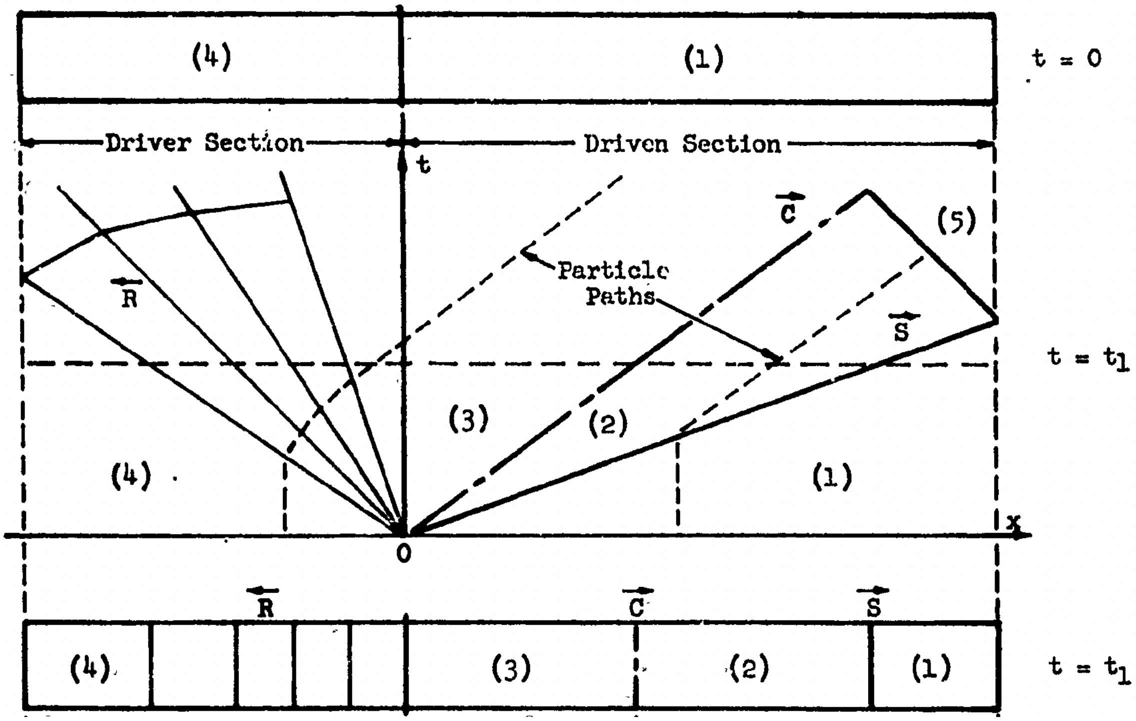

Figure 1.5: Typical shock tube x-t diagram. (Martin 1968)

With a converging-diverging nozzle, HXT becomes a reflected-shock tunnel, seen in Figure 1.6. The entrance to the nozzle is a stagnation region and causes a reflection [5]. Reflected-shock tunnels allow for longer test times, almost ten times that of an expansion tunnel [6]. This is because the shock wave reflecting from the nozzle and back into the oncoming flow interacts with and slows down the contact surface [1]. A wave diagram can be seen in Figure 1.7. This test time though, is limited by the arrival of the initial shock at the nozzle and the return of the wave after the reflected primary shockwave interacts with the contact surface. If this return of the wave can be stopped, instead making conditions such that the reflected shockwave passes through the contact surface, test times can be increased even more, as much as 3 times that of the regular reflected shock tunnel [1]. This is called "tailoring" and is achieved by making the driver and driven gases behind the shock wave match in both pressure and velocity [1].

The test section Mach number is however, typically fixed by the nozzle itself; a Mach 8 nozzle cannot produce Mach numbers beyond 8. The TAMU Actively Controlled Expansion (ACE) nozzle, a planar nozzle design, has the potential to eliminate this limitation by allowing its throat to change in height. Though, there are flow quality challenges associated with this design.

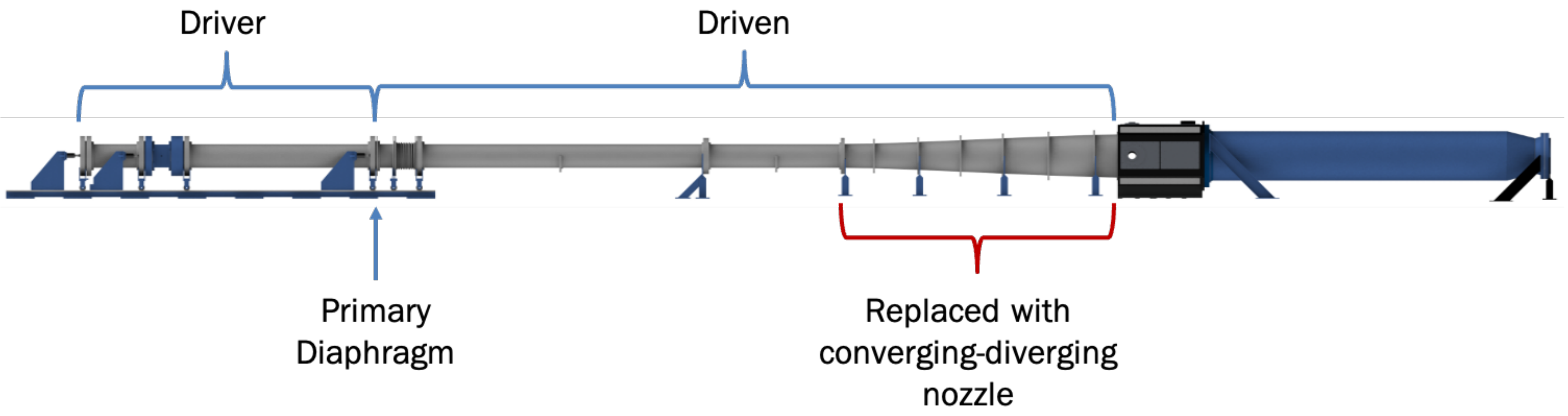

Figure 1.6: Reflected shock tunnel configuration of HXT with parts labeled.

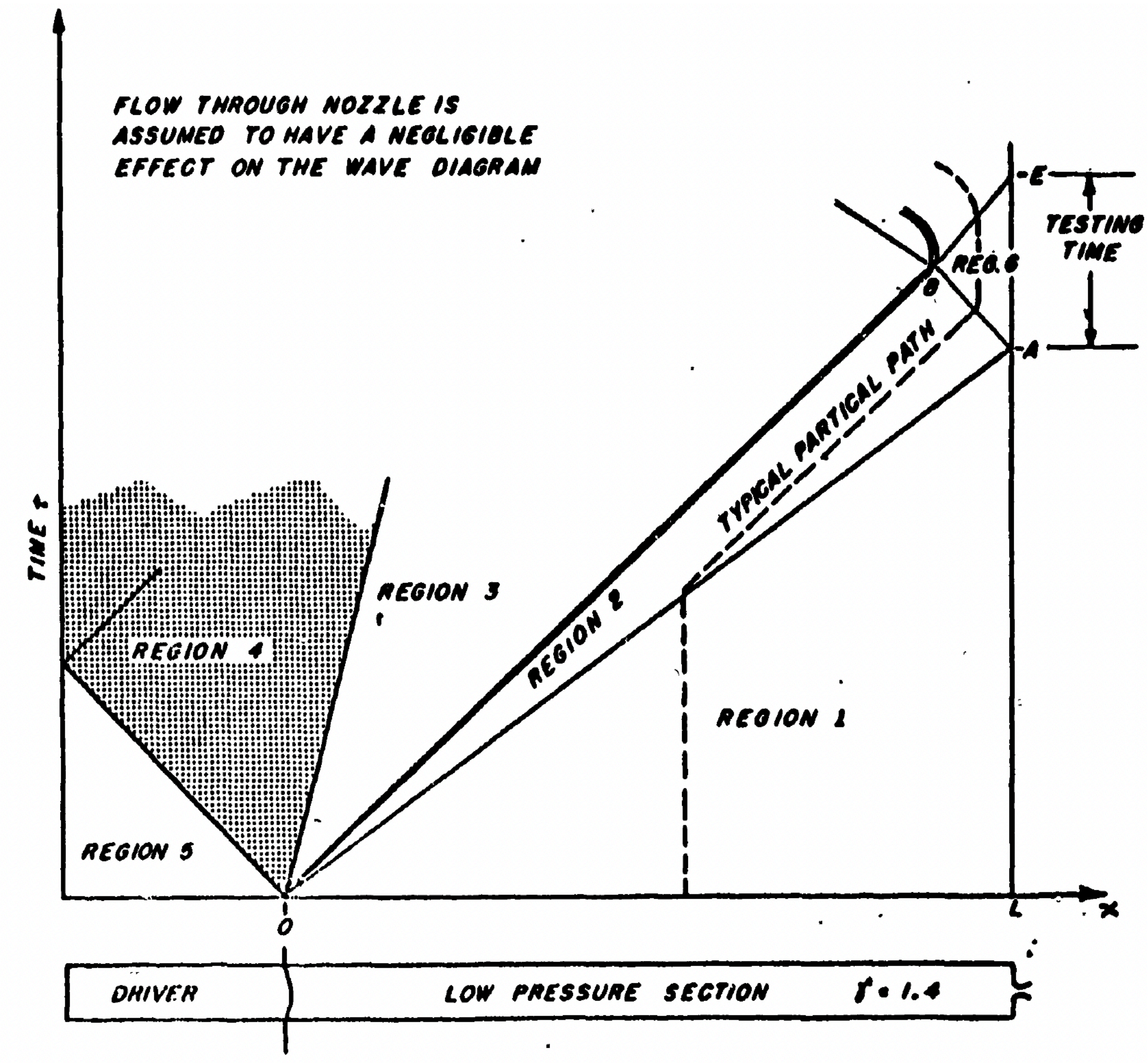

Figure 1.7: Typical reflected shock tunnel x-t diagram. (Martin 1968)

1.2.2 Nozzle Types

The two types of nozzles that this paper looks at are referred to as "planar" and "axisymmetric". The planar nozzle discussed here is made of two walls machined in the shape of the nozzle enclosed by two straight walls to create a boxlike cavity for the air to flow through making a rectangular cross section that is symmetric about the stream-wise planes. The axisymmetric nozzle is a cylindrical nozzle and has a circular cross section and is symmetric about the stream-wise axis.

The planar nozzle designed for HST will be an ACE type, meaning that it is based off the existing ACE nozzle at the NAL. This facility has the unique ability to alter its exit Mach number by changing the height of the throat while keeping the exit dimensions the same. This is accomplished by applying force on the upstream end of the nozzle which causes a rigid rotation around the flexure at the downstream end of the nozzle [7]. A schematic can be seen in Figure 2.1. Similarly, the HST planar nozzle will allow for this throat height change to occur. This allows HST to continue producing a range of Mach numbers regardless of the configuration the tunnel is in. Unfortunately, for hypersonic planar nozzles, it is hard to hold the dimensional stability of the throat steady [8] because the throat height is made to be small to obtain the exit area ratio needed [9]. Planar nozzles also have flow disturbing vortices shed from the corners [10] that must be accounted and corrected for. This is beyond the scope of this study though.

Axisymmetric nozzles tend to be best suited for hypersonic flow because the throat size is not as small as its planar counterpart (this can be seen in Table 3.1 for the two types of nozzles discussed later in this paper). The main downside to axisymmetric nozzles is the lack of ability to change the exit Mach number; a new axisymmetric nozzle must be made for each exit Mach number desired [8]. For HST, the existing infrastructure is axisymmetric, as can be seen in the figures showing HXT, making integration much simpler than it would be for a planar nozzle.

1.2.3 Other Considerations

1.2.3.1 Real Gas Effects

With shock wave speeds exceeding Mach 3, ideal gas can no longer be assumed for the fluid in the tunnel. The ratio between specific heats lowers from its ideal state at 1.4 for air. At around 2,000 K, air begins to disassociate and become more excited, leading to chemical reactions. Martin [1] goes into more detail about this process and its effects. He lists that because the decrease in temperature behind the shock wave is higher for real gas than ideal, that higher Mach numbers are achievable than what is predicted using the ideal gas assumption.

1.2.3.2 Heat Transfer

The highest heat fluxes and temperatures can be expected at or near the throat of a nozzle [11]. Due to this, there was concern for the erosion of the nozzle throat caused by the melting of the material in this area. However, even if melting temperatures are reached at the surface of the wall, since the run times are so short, the heat does not penetrate into the wall very far and the amount of material melted is not significant [12].

1.3 Research Objectives

The objective of this work is to further expand HXTs ability to include a reflected-shock tunnel mode to allow for longer test times and the removal of the complexity associated with the secondary diaphragm encountered in the expansion tunnel mode. A converging-diverging nozzle is needed to achieve this. The work presented is over the comparison of axisymmetric and planar converging-diverging nozzles of various exit Mach numbers. The results will be used to determine the best design for the new HST.

2. APPROACH

2.1 Method of Characteristics

The ACE nozzle concept is illustrated schematically in Figure 2.1. To control the Mach number, the throat height is varied by a rigid rotation of the contoured nozzle surfaces about flexures at the nozzle exit. This approach was based on the observation that at high Mach numbers, the contour shape in the downstream portion of the nozzle is similar across a relatively wide Mach number range, the nozzle performance is controlled by the initial turning angle, and the initial wall angle upon rotation can be approximately matched to the exact MOC value by controlling the design point Mach number and the number of reflections of the initial turning angle expansion before performing wave cancellation in the downstream portion of the of the nozzle. An advantage of this approach is that only small rotations are required to accomplish the desired Mach number variation.

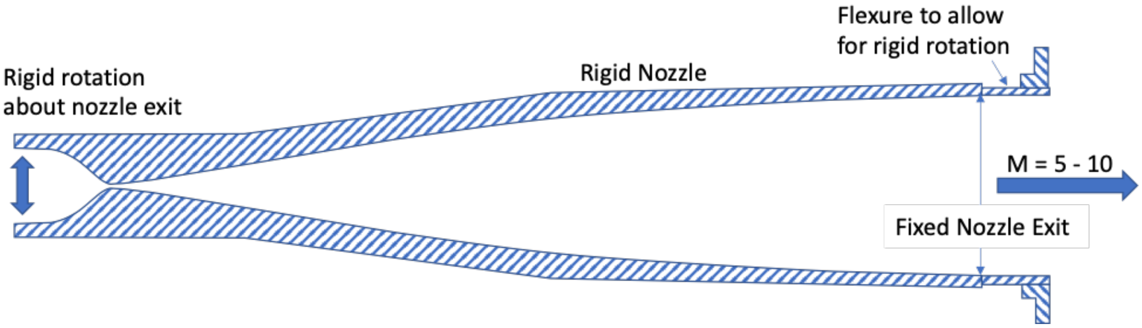

Figure 2.1: Schematic showing the ACE tunnel concept.

The nozzles were designed with two in-house MOC codes developed by the PI Dr. Bowersox. The planar nozzle MOC code follows the procedures described in Anderson [13] with the addition of a finite radius throat and multiple reflections of the expansion fan before cancelling for a uniform exit. The planar nozzle design was optimized to operate over a Mach number range of 6 to

10. This was accomplished by designing around an intermediate Mach number such that, when rotated for off-design operation at different Mach numbers, the difference in the initial turning angle was minimized as compared to the exact MOC design. For these calculations, the MOC codes were numerically converged. The solutions include 100 characteristics and multiple reflections to control the initial wall angle. An example MOC nozzle design is summarized in Figures 2.2 and 2.3. The design point is selected to minimize the difference between the actual and rotated nozzle angles. The resulting rotated nozzle contours are compared to the exact MOC results, illustrated in Figures 2.4 to 2.6. These results show that the initial turning region near the throat is closely approximated by the rotated nozzle. An iterative analysis between the CFD and MOC calculations was performed to determine an effective nozzle truncation point that balances viscous effects and exit flow angle.

In Figure 2.2, the dashed line is the estimated boundary layer thickness and in Figure 2.3, the dots indicated the location of the characteristics intersections, which is where the flow properties are computed. The following three pictures have the rotated Mach 9.2 nozzle represented as the red dashed line and the exact MOC nozzle for the Mach number as the black line.

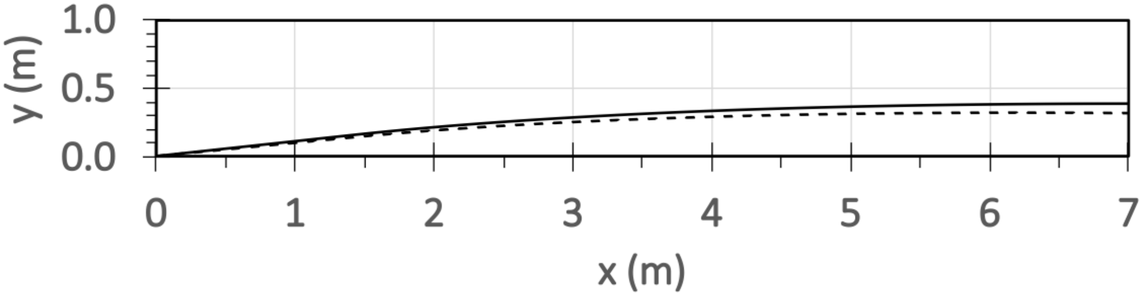

Figure 2.2: MOC wall contour with viscous displacement thickness estimate.

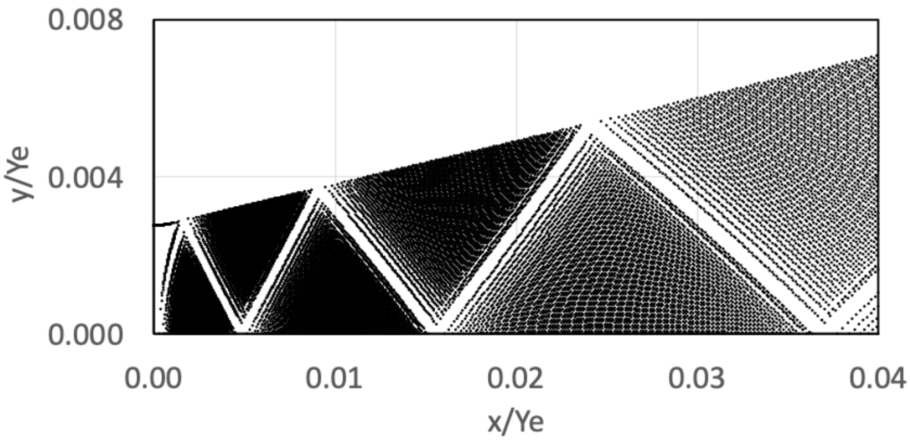

Figure 2.3: MOC mesh in the throat region.

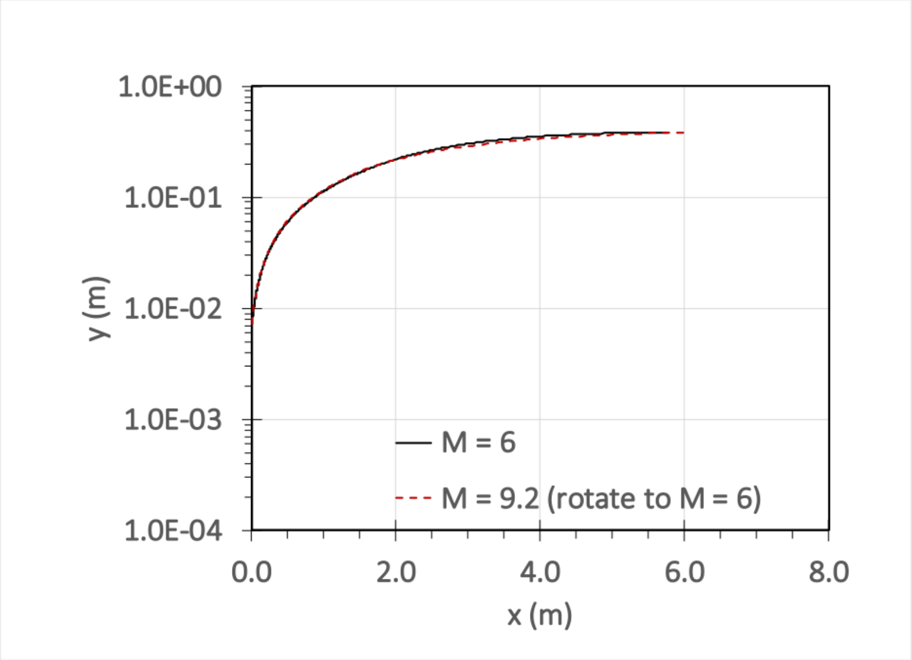

Figure 2.4: Comparison of rotated optimum nozzle to exact MOC nozzle contour for Mach 6.

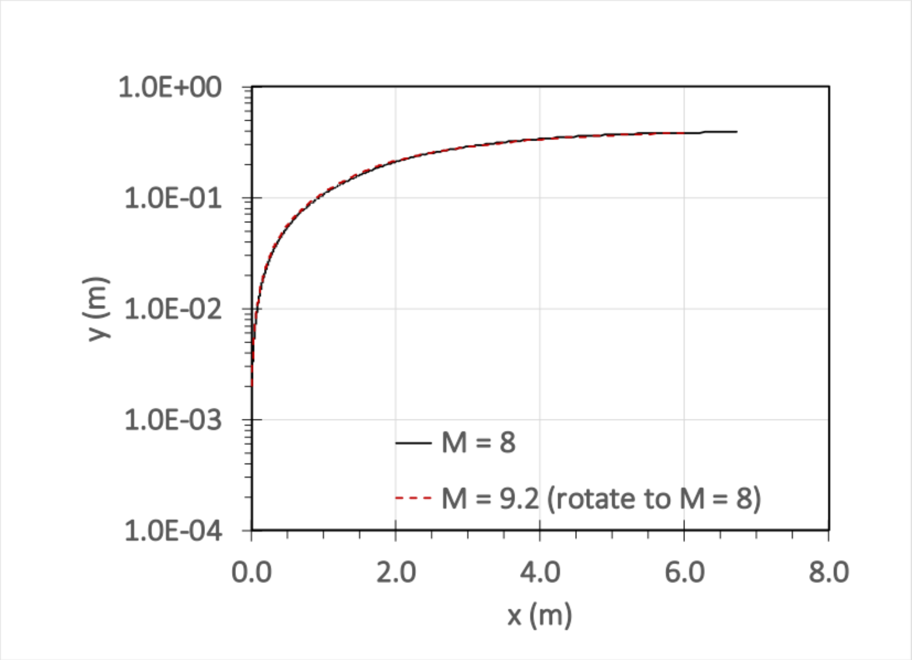

Figure 2.5: Comparison of rotated optimum nozzle to exact MOC nozzle contour for Mach 8.

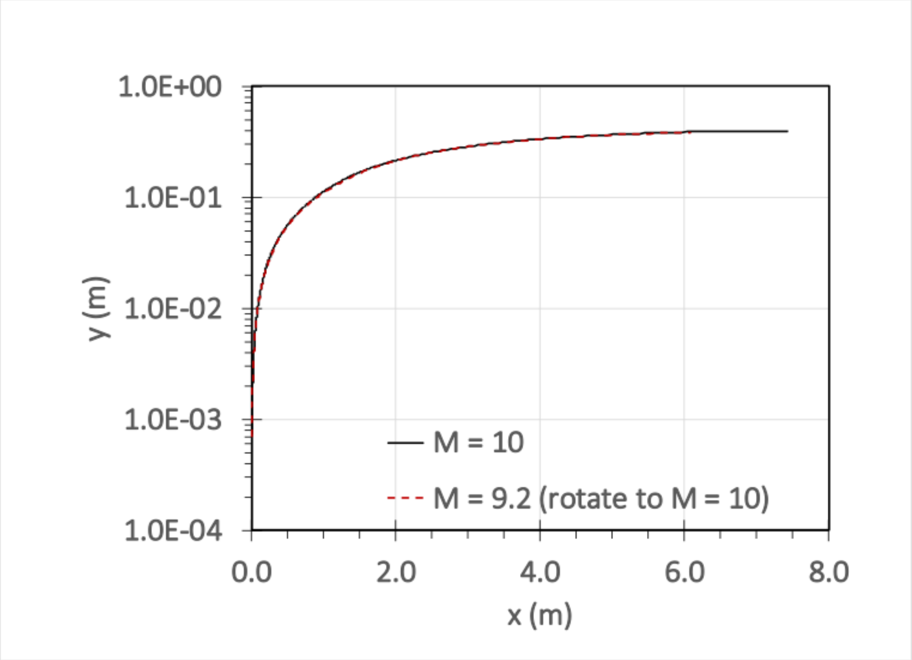

Figure 2.6: Comparison of rotated optimum nozzle to exact MOC nozzle contour for Mach 10.

The axisymmetric nozzle MOC code follows the procedures described in Zucrow and Hoffman [14] with the addition of multiple reflections of the expansion fan before cancelling for uniform exit. The axisymmetric nozzle designs were at fixed Mach number. For these calculations, the MOC codes were numerically converged. The solutions include 200 characteristics and multiple reflections to control the initial wall angle. An example MOC nozzle design for the HXT facility is given in Figures 2.7 and 2.8. The first figure shows the characteristic mesh an example axisymmetric MOC results with a streamline contour, in yellow, of the diverging HXT nozzle.

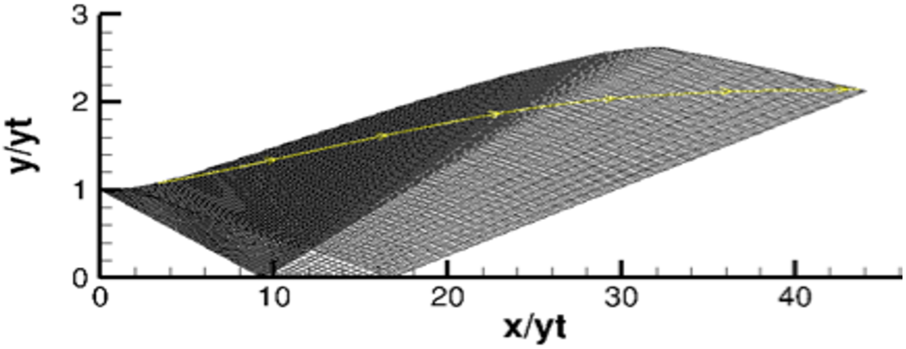

Figure 2.7: Characteristic mesh of an example axisymmetric code with the y-axis exaggerated to better show the characteristics.

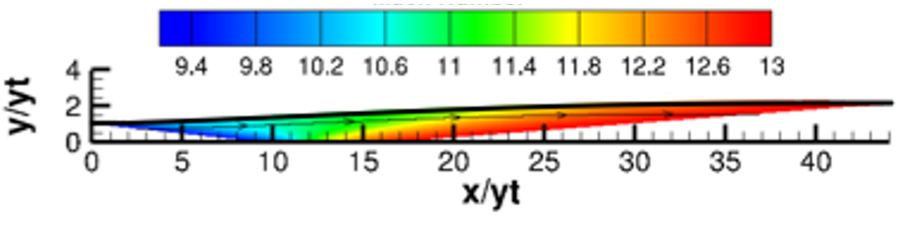

Figure 2.8: Mach number map for the HXT nozzle design.

The available design tools only produce the supersonic section of the nozzle design, so an additional code was required to add the subsonic section. These converging sections were generated by a MatLab code written by PhD student Joseph Carlson. This code uses a cubic polynomial with known boundary conditions. Five constraints are imposed to completely define the cubic polynomial. At the furthest upstream point, the height is determined to be equal to the height of the supersonic nozzle exit. The distance from the throat is determined by eye to give sufficient distance for flow convergence. The third constraint is the location of the throat into the supersonic section of the nozzle. The last two constraints imposed are that the slope of the subsonic nozzle is zero at both the entrance to the subsonic section and at the throat. This method has been used for many other converging-diverging nozzles, and CFD results indicate that the generated flow field is as desired.

Once the curves were complete, they were exported into Solidworks in order to be converted into a more useful format for grid generation.

2.2 Computational Fluid Dynamics

Pointwise, a commercial meshing software, was used to create the 2D grids of the nozzles. Three different meshes of varying density were generated for each curve; a coarse, a mid-range, and a fine mesh were created for the curves, each having double the amount of grid points as the last. Table 2.1 details the amount of points each grid had in the streamwise, x, and transverse, y, directions, the x-direction further split on either side of the throat. By having three meshes of different density, computational run times are significantly reduced. This was done by using the solution of the less dense mesh as the initial guess of the next higher density mesh; i.e. the coarse solution was used as an initial guess of the medium grid.

Grid Density	Horizontal Subsonic/Supersonic	Vertical
Coarse	25/125	50
Mid	50/250	100
Fine	100/500	200

Table 2.1: Grid point allocation for different mesh densities.

Because the CFD runs were viscous, the meshes had points distributed in higher density towards the wall to capture the boundary layer. Likewise, in order to account for the expansion at the throat, points were distributed towards it from both subsonic and supersonic sides. Figure 2.9 shows an example of the coarse grid for the Mach 6 axisymmetric nozzle and the distribution of the cells.

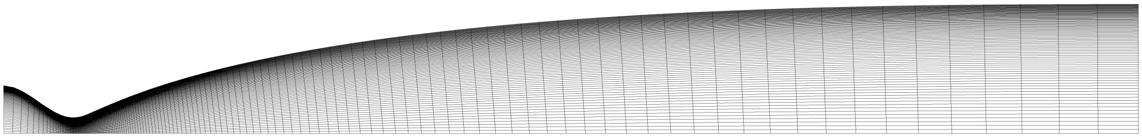

Figure 2.9: Axisymmetric Mach 6 coarse mesh with y-axis exaggerated to better showcase the individual cells.

The boundary conditions differed between nozzle type only on the lower boundary, shown as line BC in Figure 2.10. For the axisymmetric cases, this line was denoted as the axis, and for the planar cases, this line represented a symmetry plane. Other boundary conditions included the inlet (line AB), outlet (line CD), wall (line AD), and symmetry plane (plane ABCD), which stayed the same for all nozzles.

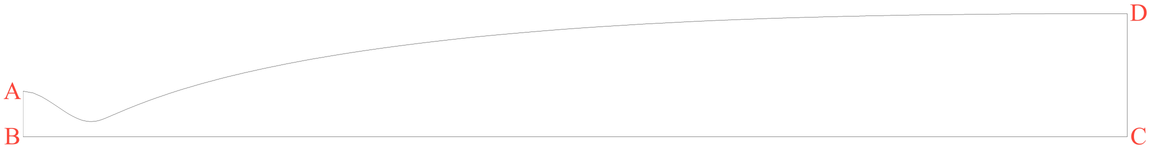

Figure 2.10: Axisymmetric Mach 6 boundary lines.

ANSYS Fluent, a commercial software, was used on the ADA supercomputer. ADA is a hybrid cluster from IBM/Lenovo and has 856 compute nodes and 8 login nodes. Access to ADA is available to any TAMU student and is done using a secure shell session or ssh through any ssh capable terminal or program.

Fluent has two options for solvers, a pressure-based and a density-based solver. For the runs discussed in this paper, the steady-state density-based RANS solver was used. The paper was not concerned with transient behavior which is why steady-state was used. The density-based solver is better for high-speed compressible flows than the pressure-based solver and RANS was used to capture the boundary layer growth.

The coupled-implicit formulation was the chosen algorithm to simultaneously solve the coupled equations. Implicit is typically faster to converge and more stable than explicit formulation.

The convective flux type used with this density-based solver was the ROE-FDS, which is the default and worked well. This scheme uses an Approximate Riemann Solver to calculate the fluxes [15].

The standard k-omega model was the turbulent model used in these CFD simulations, which in Fluent is based on the Wilcox k-omega model. This model has modifications for low Reynolds number effects, compressibility, and shear flow spreading [15]. This model is more accurate for internal flows than others.

Additional simulation parameters included assumption of air following the ideal gas law, boundary conditions of an isothermal wall, pressure inlet and outlet (outlet switches to vent when supersonic), and symmetry on the side (x-y) planes. The ideal gas assumption was determined to not be applicable for these runs and additional computational fluid dynamics simulations are recommended for the Mach 8 axisymmetric nozzle using air as a non-ideal gas. However, the effects caused by real gas are considered to be small due to gamma only changing to 1.3 from the ideal at 1.4.

The initial conditions used are listed in Table 2.2. Stagnation conditions were used because the flow stagnates at the inlet of the nozzle.

Mach Number	Stagnation Pressure [MPa]	Stagnation Temperature [K]
6	12.82	1800
8	6.07	3040
10	2.23	4625

Table 2.2: Run condition inputs for Fluent.

2.3 Computer Aided Design

The mechanical design of an ACE type variable Mach number planar nozzle and a Mach 8 axisymmetric nozzle were designed using the commercial CAD software Solidworks. The design of each nozzle had to fit into existing infrastructure of HXT. Most notably limiting are the length of the nozzles and the exit size. The nozzles must fit between the acceleration pipe and the test section, their exits must fit into the existing test section inlet, they must seal against both pressure and vacuum, and they must be able to be supported in the same locations as the current expansion nozzle to avoid compromising the integrity of the lab floor. Figures 2.11 and 2.12 illustrate the dimensions that the new nozzle must conform to. The dimensions in the figures are in meters.

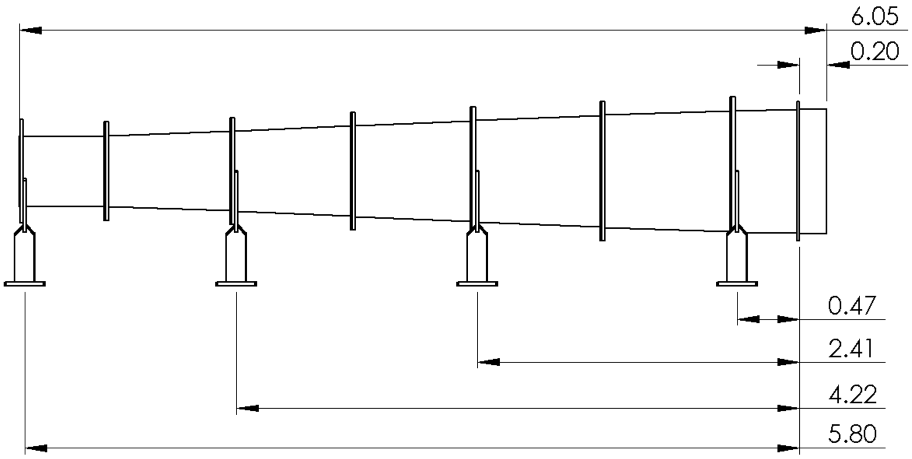

Figure 2.11: Current HXT expansion nozzle dimensions.

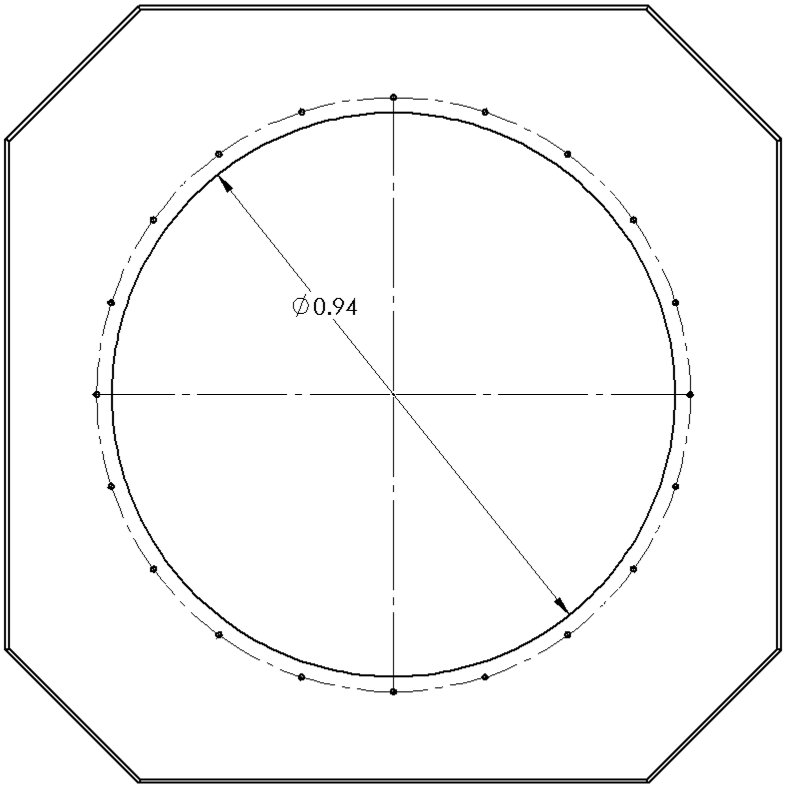

Figure 2.12: Test section inlet.

2.4 Heat Transfer

Heat conduction calculations were preformed on the wall of the throat of the Mach 8 axisymmetric nozzle to better understand what kind of material would be able to handle the high temperatures associated with the throat. The throat was simulated as a semi-infinite solid with a constant heat flux applied to its surface. The heat flux was obtained from the CFD data and the equations used came from Holman's Heat Transfer book [11].

The initial and boundary conditions are listed as equations 2.1 and 2.2 respectively.

$$T(x,0) = T_i \tag{2.1}$$

$$Q = -k\frac{\partial T}{\partial x}|_{x=0} \tag{2.2}$$

The solution for this problem is shown as equation 2.3 below, with T being the variable of interest.

$$T - T_i = \frac{2Q\sqrt{\frac{\alpha\tau}{\pi}}}{k} exp(\frac{-x^2}{4\alpha\tau}) - \frac{Qx}{k}(1 - erf(\frac{x}{2\sqrt{\alpha\tau}})) \tag{2.3}$$

A Matlab code was written with heat flux, the thermal properties of the material, and time as inputs, with the user choosing a material to begin with. This code outputs the temperature of the surface of the wall at 30 milliseconds, the time it takes for the surface to reach the melting temperature of the material, and a graph depicting the heat transfer 2.54 centimeters into the wall at various times.

3. RESULTS

3.1 Computational Fluid Dynamics

The cases considered were designed to reach an exit Mach number of 6, 8, and 10. Discussed in the following are the CFD results of these nozzle designs with Table 3.1 listing their dimensions below. The planar nozzle dimensions listed are half height and the axisymmetric values listed are radius. As was discussed earlier, the throat for the planar case is much smaller than its axisymmetric counterpart.

Nozzle Type	Design Mach Number	Throat [cm]	Inlet [cm]	Exit [cm]
Planar	6	0.38	5.08	20.32
Planar	8	0.10	5.08	20.32
Planar	10	0.03	5.08	20.32
Axisymmetric	6	6.20	18.57	50.00
Axisymmetric	8	3.18	18.57	50.00
Axisymmetric	10	1.78	18.57	50.00

Table 3.1: Nozzle dimensions.

3.1.1 Mach 6

3.1.1.1 Planar Nozzle

Convergence was said to be reached when the residuals fell 8 orders of magnitude for the planar Mach 6 nozzle. Below, Figures 3.1 to 3.3 show pressure throughout the nozzle as well as the x and y components of velocity, u and v respectfully. Additionally, Figure 3.4 shows the Mach number through the nozzle and Figure 3.5 illustrates the grid independence study, showing that each mesh reached the same exit Mach number independently. An exit core Mach number for this nozzle is an average of 5.86. This lower Mach number than the designed is attributed to the underestimation of the viscous displacement in the MOC used to create this nozzle; the boundary layer was larger than what the MOC predicted.

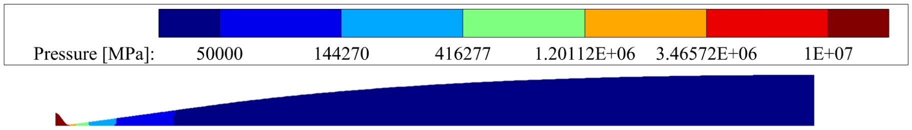

Figure 3.1: Planar Mach 6 nozzle pressure field.

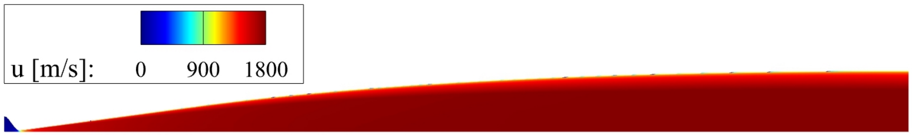

Figure 3.2: Planar Mach 6 nozzle x-component velocity.

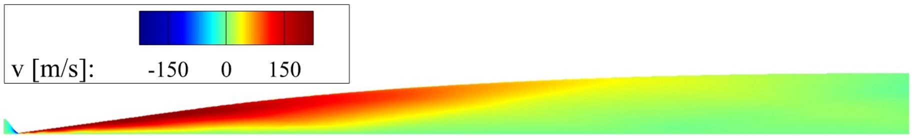

Figure 3.3: Planar Mach 6 nozzle y-component velocity.

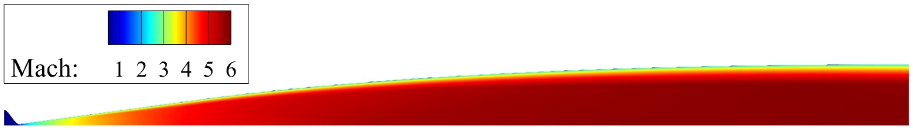

Figure 3.4: Planar Mach 6 nozzle Mach number.

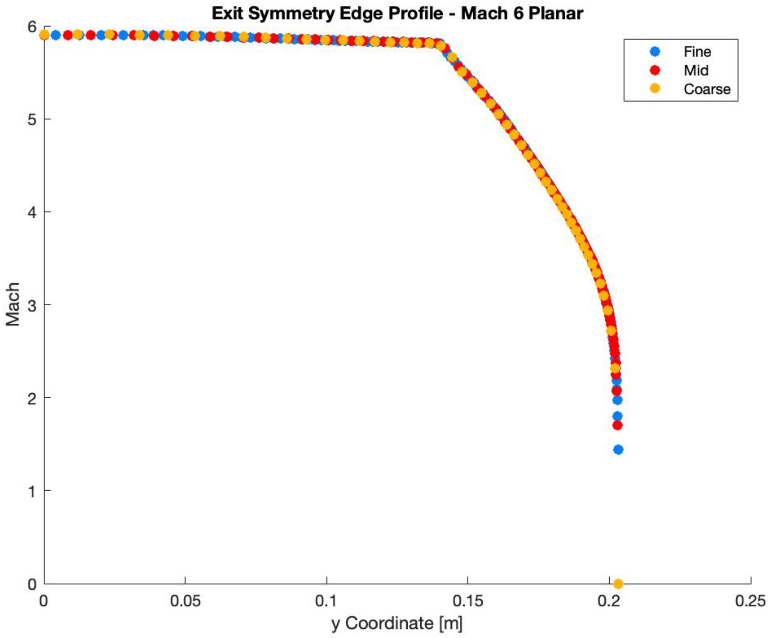

Figure 3.5: Planar Mach 6 nozzle grid independence study.

3.1.1.2 Axisymmetric Nozzle

A Mach 6 axisymmetric nozzle was simulated in Fluent for comparison with the planar case. Convergence was reached with a drop in the residuals of 6 orders of magnitude. Similar figures to the planar case are shown below in Figures 3.6 to 3.10. Exit core Mach number for this nozzle is an average of 6.15, slightly higher than its design and planar counterpart. This overshoot is due to the overestimation of the viscous displacement, the exact opposite of what occurred with the planar nozzle. The boundary layer here was smaller than the MOC predicted.

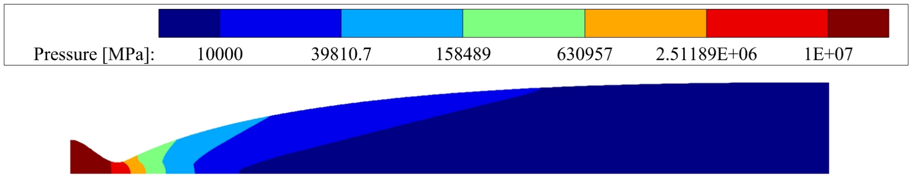

Figure 3.6: Axisymmetric Mach 6 nozzle pressure field.

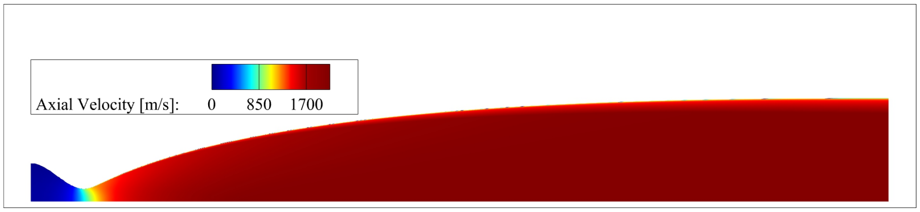

Figure 3.7: Axisymmetric Mach 6 nozzle axial-component velocity.

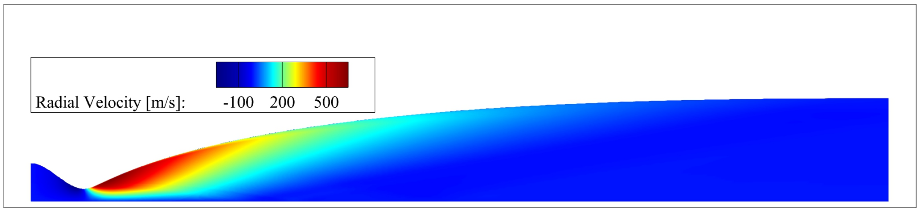

Figure 3.8: Axisymmetric Mach 6 nozzle radial-component velocity.

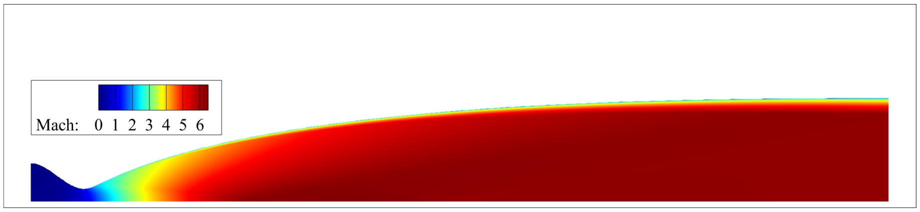

Figure 3.9: Axisymmetric Mach 6 nozzle Mach number.

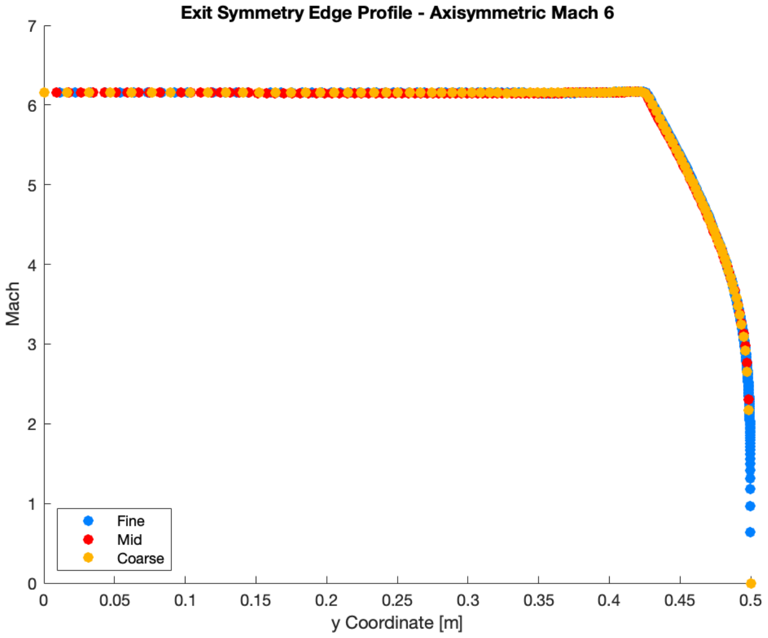

Figure 3.10: Axisymmetric Mach 6 nozzle grid independence study.

3.1.1.3 Comparison

Boundary layer (BL) thickness was measured to be from the wall to where the stream-wise velocity reached 99% of the core flow value. The boundary layer for the axisymmetric is larger than the planar boundary layer but the loss in core flow area is much smaller than the planar counterpart. This is due to the physical size of the axisymmetric nozzle being much larger than the planar.

Nozzle Type	Design Mach #	Exit Mach #	BL Thickness [cm]	Loss from BL
Planar	6	5.86	6.07	29.88%
Axisymmetric	6	6.15	6.91	13.81%

Table 3.2: Mach 6 nozzle CFD results.

3.1.2 Mach 8

3.1.2.1 Planar Nozzle

These are preliminary results for the planar Mach 8 nozzle as there was complexities causing the solution to not converge completely, which can be seen in the grid independence study in Figure 3.15 where there is disagreement between meshes on the final answer.

Below, Figures 3.11 to 3.13 show pressure throughout the nozzle as well as u and v velocity. Additionally, Figure 3.14 shows Mach number through the nozzle. An exit core Mach number for this nozzle is an average of 7.57, the viscous displacement greatly underestimated.

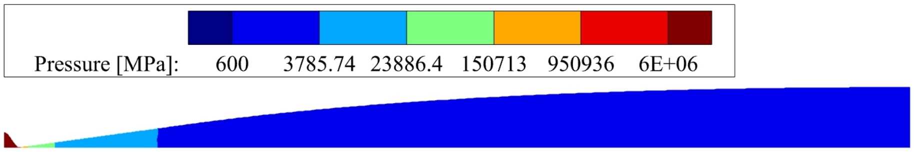

Figure 3.11: Planar Mach 8 nozzle pressure field.

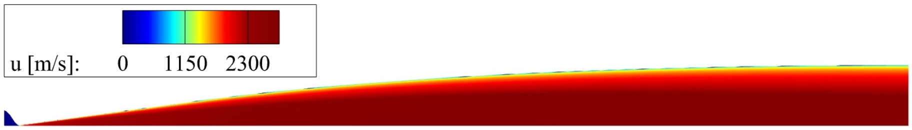

Figure 3.12: Planar Mach 8 nozzle x-component velocity.

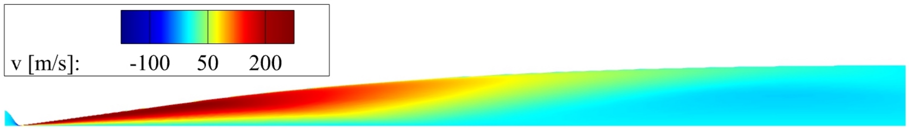

Figure 3.13: Planar Mach 8 nozzle y-component velocity.

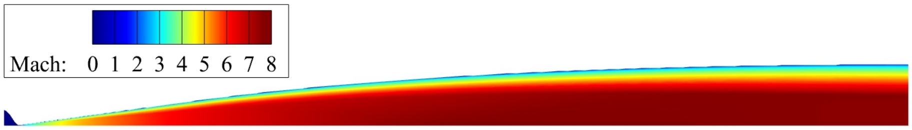

Figure 3.14: Planar Mach 8 nozzle Mach number.

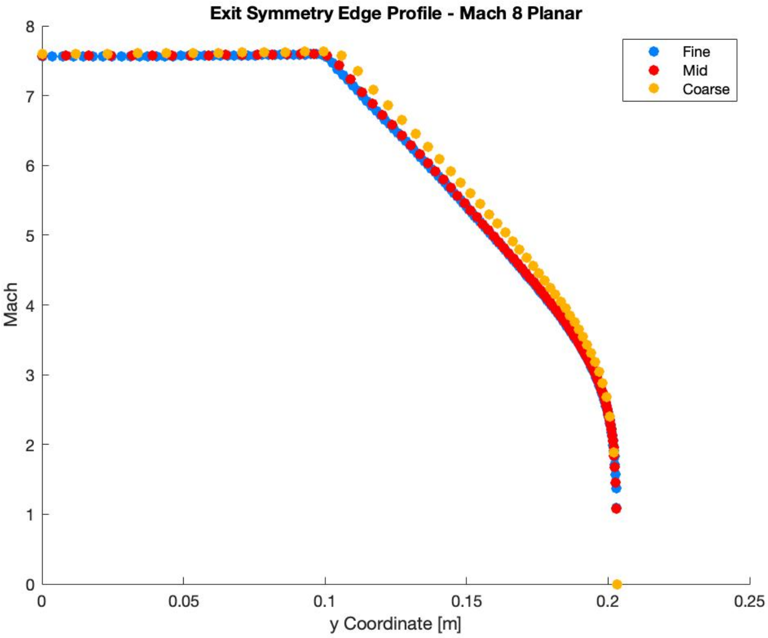

Figure 3.15: Planar Mach 8 nozzle grid independence study.

3.1.2.2 *Axisymmetric Nozzle*

A Mach 8 axisymmetric case was simulated for comparison. Convergence was reached with a drop in the residuals of 6 orders of magnitude. Similar figures as the Mach 6 cases are shown below in Figures 3.16-3.20. Exit core Mach number for this nozzle is an average of 8.04, the MOC having predicted a boundary layer thickness close to the simulated one.

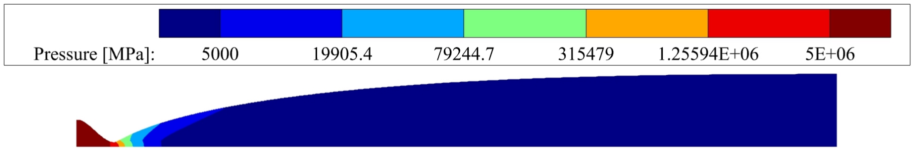

Figure 3.16: Axisymmetric Mach 8 nozzle pressure field.

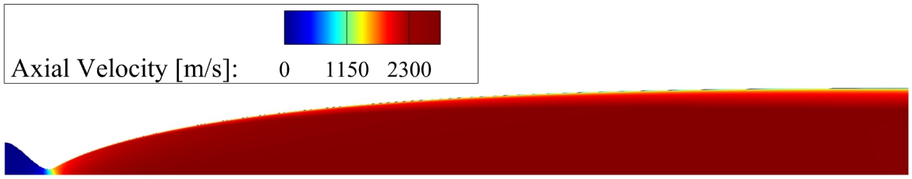

Figure 3.17: Axisymmetric Mach 8 nozzle axial-component velocity.

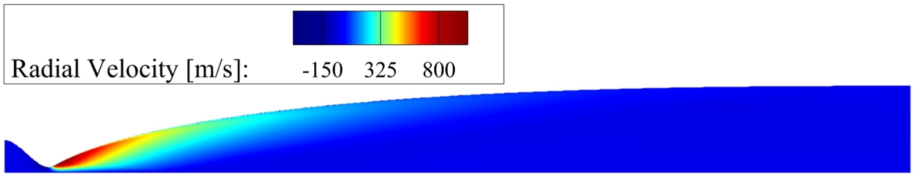

Figure 3.18: Axisymmetric Mach 8 nozzle radial-component velocity.

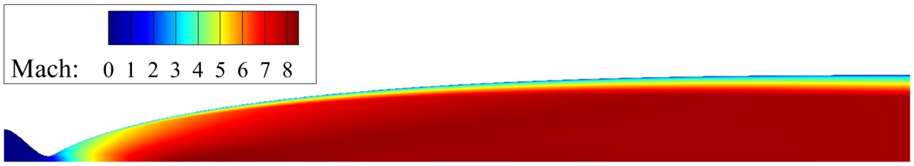

Figure 3.19: Axisymmetric Mach 8 nozzle Mach number.

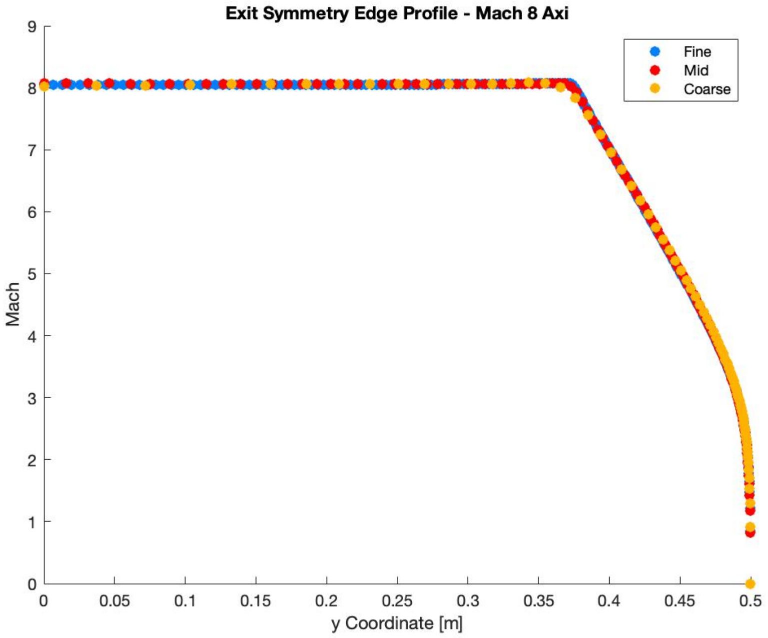

Figure 3.20: Axisymmetric Mach 8 nozzle grid independence study.

3.1.2.3 Comparison

The boundary layer is larger here for the axisymmetric nozzle, but the loss in core flow area is almost half of the planar. Again, this is attributed to the larger size of the axisymmetric nozzle compared to the planar nozzle.

Due to the issues of convergence discussed before, it should be noted that the planar results may not be accurate.

Nozzle Type	Design Mach #	Exit Mach #	BL Thickness [cm]	Loss from BL
Planar	8	7.57	9.83	48.38%
Axisymmetric	8	8.04	12.45	24.89%

Table 3.3: Mach 8 nozzle CFD results.

3.1.3 Mach 10

3.1.3.1 Planar Nozzle

Further investigation into higher Mach number planar nozzles was not undertaken due to the results of the planar Mach 6 and 8 nozzle. These results clearly show that the boundary layer in the planar nozzle takes up a significant portion of the exit area and will only get thicker as the Mach number is increased.

3.1.3.2 Axisymmetric Nozzle

For the axisymmetric Mach 10 nozzle, convergence was reached with a drop in the residuals of 5 orders of magnitude. Similar figures as the Mach 10 planar cases are shown below in Figures 3.21 to 3.25. Exit core Mach number for this nozzle is an average of 9.69, which, unlike the previous axisymmetric nozzles, is lower than the design Mach number. This is because of the thick boundary layer and due to the underestimation of the viscous effects in the MOC used to design this nozzle.

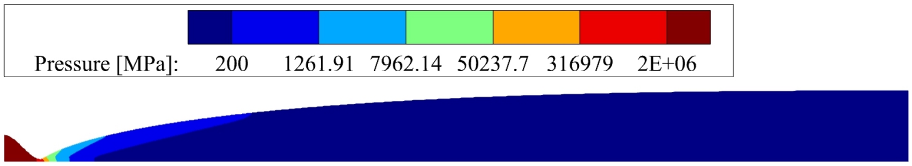

Figure 3.21: Axisymmetric Mach 10 nozzle pressure field.

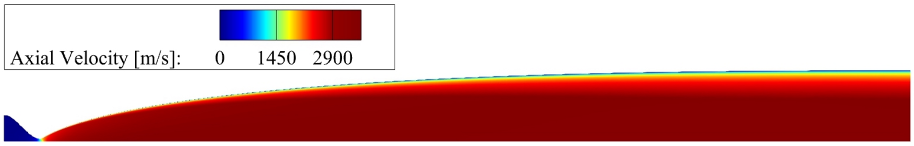

Figure 3.22: Axisymmetric Mach 10 nozzle axial-component velocity.

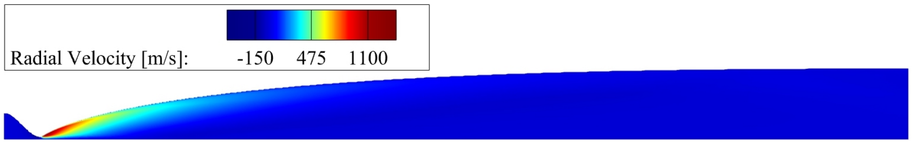

Figure 3.23: Axisymmetric Mach 10 nozzle radial-component velocity.

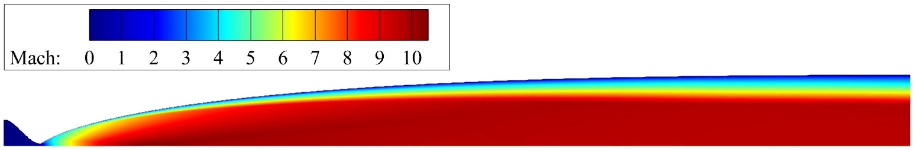

Figure 3.24: Axisymmetric Mach 10 nozzle Mach number.

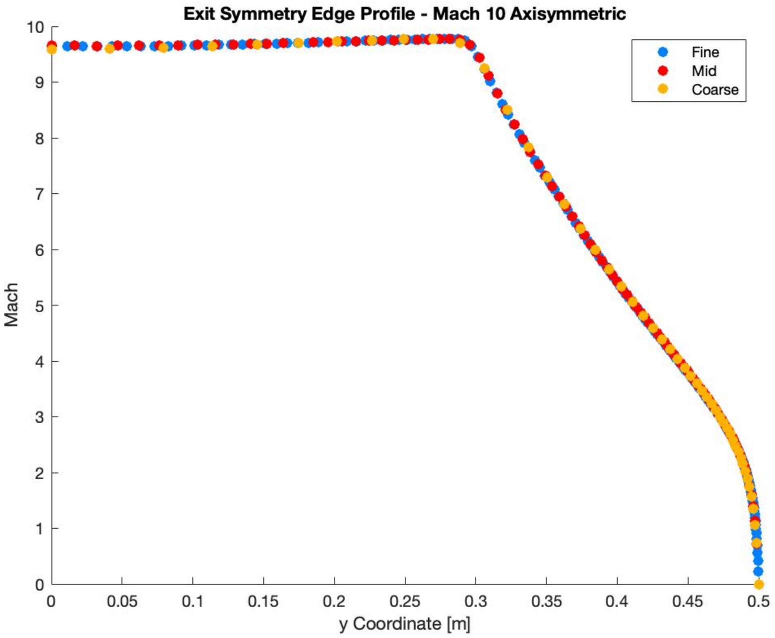

Figure 3.25: Axisymmetric Mach 10 nozzle grid independence study.

3.1.3.3 Comparison

The results for the axisymmetric case are still listed in Table 3.4 below. Unlike the the other axisymmetric cases, the Mach 10 nozzle produces a smaller exit Mach number than the design. It also has the largest BL and therefore the largest loss in core flow area.

Nozzle Type	Design Mach #	Exit Mach #	BL Thickness [cm]	Loss from BL
Axisymmetric	10	9.69	19.38	38.75%

Table 3.4: Mach 10 nozzle CFD results.

3.2 Computer Aided Design

Overall, the lengths of the nozzles did not pose a challenge since all curves produced were less than the maximum allotted size. However, the axisymmetric and the planar nozzles differed in their issues with the other three constraints: support stand locations, outlets fitting into the test section inlet, and sealing. In chapter 2, the current expansion nozzle of HXT is shown demonstrating the constraints the new nozzle must meet. The length between the test section and the upstream acceleration pipe is about 5.87 meters (the current nozzle extends 0.2 meters into the test section) shown in Figure 2.11. The stand locations are also shown in Figure 2.11 as distance from the test section outer wall to their midpoint. The test section inlet is 0.94 meters in diameter, illustrated in Figure 2.12.

3.2.1 Mach 8 Axisymmetric Nozzle

Shown below in Figures 3.26 and 3.27 is the full assembly of the Mach 8 axisymmetric nozzle. This section will go into depth on the mechanical design of this nozzle. Mach 8 was chosen because it was the intermediate Mach number of the Mach numbers studied.

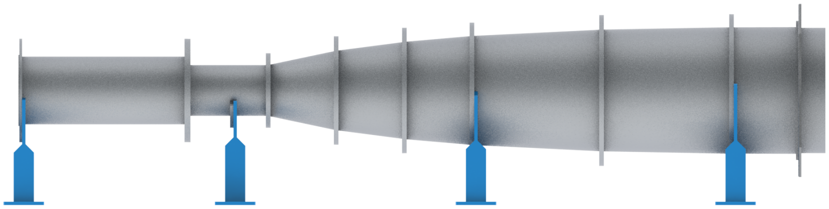

Figure 3.26: Full assembly of the Mach 8 axisymmetric nozzle.

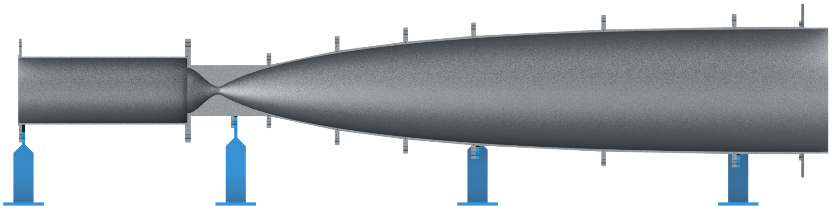

Figure 3.27: Full assembly of the Mach 8 axisymmetric nozzle, section view.

The axisymmetric nozzle is short of the 5.87 meter gap left by the removal of the current expansion HXT nozzle necessitating a 1.25 meter pipe addition to the acceleration pipe. This nozzle extends into the test section the same amount that the current nozzle does, as shown in Figures 2.11 and 3.28, bringing it to 6.05 meters in length.

The stands were able to be located in the same positions as the current nozzle, seen by comparing the figure below to Figure 2.11.

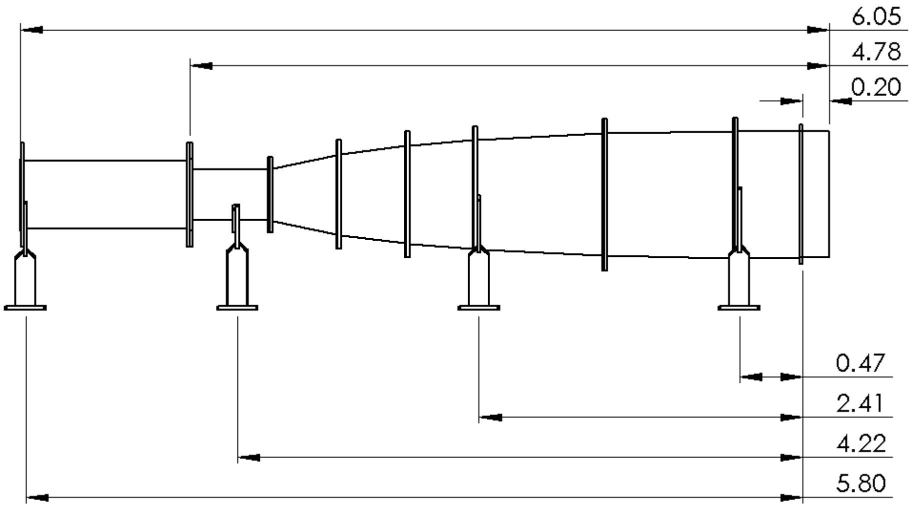

Figure 3.28: Axisymmetric nozzle dimensions.

This nozzle's exit did not fit into the test section when wall thickness was added to the contour. To remedy this, the exit cone, shown in the figure below, had material machined off the last 0.2 meters to allow it to fit into the test section. The wall of the nozzle exit is 1.27 centimeters in thickness.

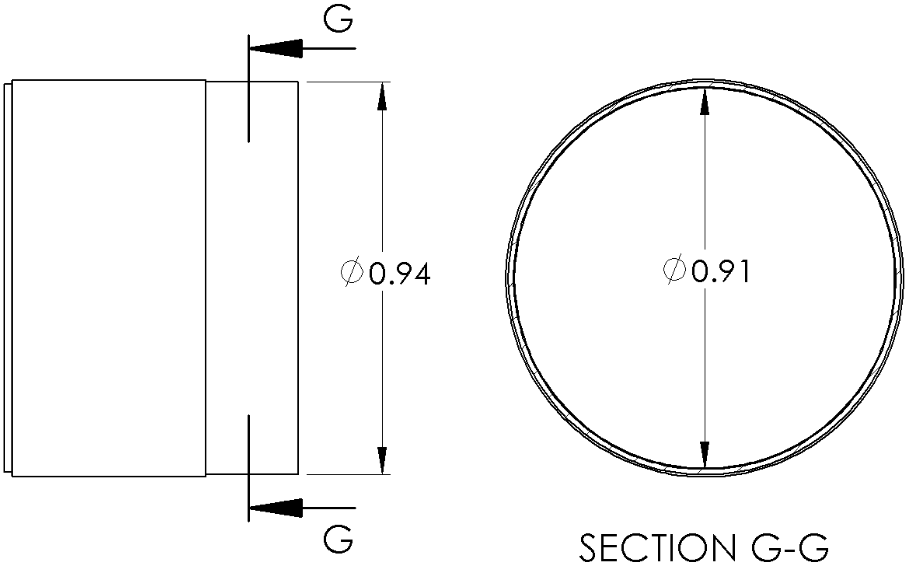

Figure 3.29: Axisymmetric exit cone.

Sealing was not an issue with this nozzle, having circular o-rings at every flange juncture shown in the figures containing the axisymmetric nozzle.

There are 6 sections of this nozzle, not including the throat. These cones will be made of 1.91 centimeter rolled stainless steel sheets that are then welded where the ends meet. The interior contour is then machined away to obtain the desired shape of the nozzle. The split locations were chosen to be located where the material machined away would be no more than 0.64 centimeters, leaving the wall thickness to a minimum of 1.27 centimeters. The downstream sections are much larger than the upstream due to the slope decreasing as the nozzle straightens out. Some cone pairs, such as, if counting from left to right, the third and fourth as well as the fifth and sixth, were split at those locations to allow for the stands to match with the current HXT stand locations. The cone lengths can be seen in Figure 3.30.

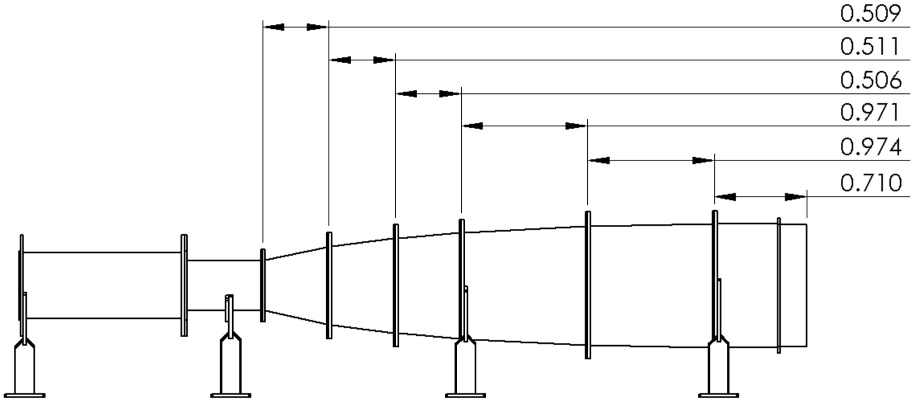

Figure 3.30: Cones of the axisymmetric nozzle.

This design, shown in full in Figure 3.26 and 3.27, includes an 1.25 meter extension of the acceleration pipe, a 0.61 meter throat section machined from a cylinder of material, and 6 conical sections making up the bulk of the nozzle. There are 16 full flanges and one-half flange. While the four stands match up with the existing stand locations, they are of different size to accommodate the different nozzle.

3.2.2 Variable Mach Number Planar Nozzle

Shown below in Figures 3.31 and 3.32 is the full assembly of the variable Mach number planar nozzle. This section will go into detail on the mechanical design of this nozzle.

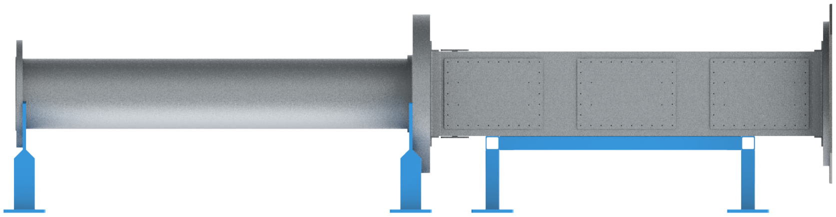

Figure 3.31: Full assembly of the variable Mach number planar nozzle.

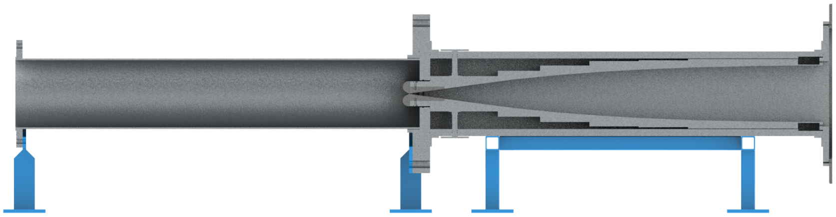

Figure 3.32: Full assembly of the variable Mach number planar nozzle, section view.

The planar nozzle is the smaller of the two designs, requiring an almost 2.9 meter extension of the acceleration pipe. This nozzle also does not extend into the test section, making the whole assembly 5.87 meters, illustrated by Figure 3.33. The nozzle inlet extends into the acceleration pipe to create a stagnation area and to help seal the outside of the nozzle from the incoming flow (seen in Figure 3.32, 3.33, and in detail in Figure 3.34).

The support stand, seen below, if counting from left to right, breaks the second constraint by being 1.2 meters further downstream than the current one. This stand is located here to hold the significant weight of the flanges that connect the acceleration pipe extension to the nozzle box.

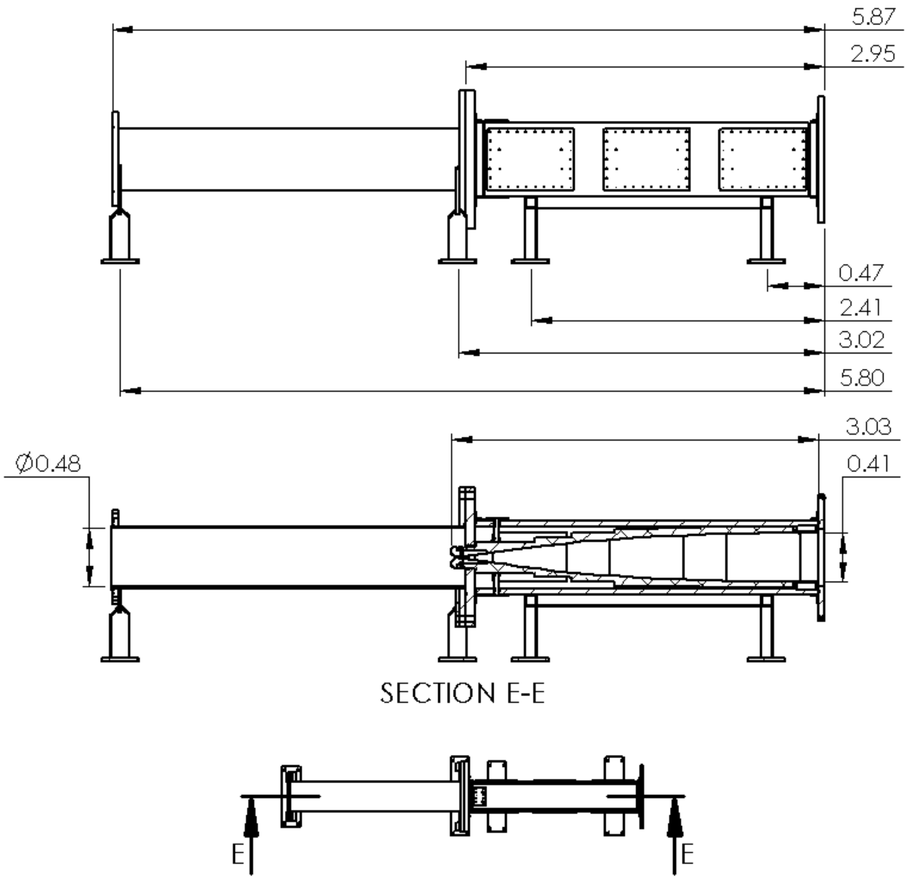

Figure 3.33: Planar nozzle dimensions.

The design of the planar nozzle holds a unique sealing challenge because of its ability for lateral movement of the throat and because it is a planar nozzle connecting to existing cylindrical parts. The planar nozzle yields Mach numbers ranging from 6 to 10 which corresponds to 0.36 centimeters of vertical movement of just one half of the nozzle throat. Sealing this becomes an issue especially at the high Mach numbers because any pressure against the sealing material near this area is reduced, lowering the effectiveness of the seal. There are two seals here to keep air from leaking into the box to help combat this issue, shown in Figure 3.34. One is the thick o-ring surrounding the throat on the inside of the flange and the other is on the face of the flange resting against a step of the nozzle wall. Both can be seen in the figure below; the thick seal is the large rectangular groove cut around the inside of the flange while the other o-ring can be seen as a small rectangular hole on the right side of the flange face that seals against one of the steps of the nozzle.

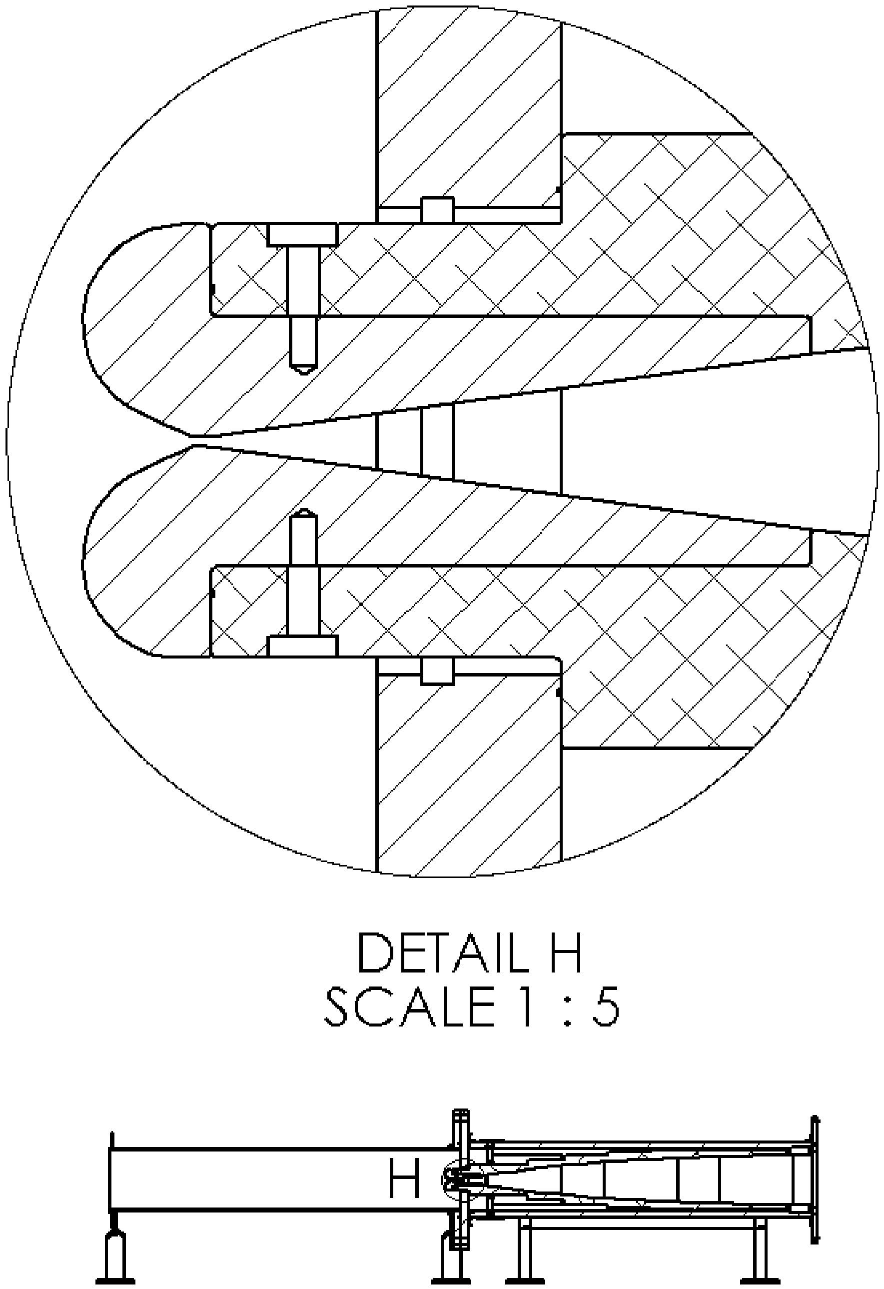

Figure 3.34: Detailed view of throat.

Sealing the flat side walls to the flanges and the contoured walls is another challenge. To be effective, an o-ring has to be continuous, have constant contact with the two pieces it is sealing, and ideally would not lay against any seams. Unfortunately, for the side walls, there is no way to truly implement an o-ring in an effective manner, not even against the flanges. The solution to this is to build a box around the nozzle and focus on sealing the box instead of the nozzle. To avoid the same problem with sealing the walls against each other, it was decided to weld the box together. Side doors were added so that access to the nozzle would still be possible for any optical, sensor, or adjustment needs. The doors can be seen on the sides of the nozzle box in Figure 3.31 and 3.33.

Here, in Figures 3.35, the o-ring groove can be seen as a small rectangular hole cut into the metal of the parts. From left to right in Figure 3.35, there is the seal between the two flanges that connect the acceleration pipe to the nozzle box, a seal between the flange to the nozzle box walls, and finally the double o-rings sealing the jack used to raise and lower the throat.

This double o-ring system on the jack was chosen because while the jack doesn't move often, it does have the ability, so the choice was made to treat it as a dynamic vacuum seal. Parker [16] recommends using a double o-ring system for such a seal. The o-ring locations on the jack are far enough away from the top and bottom edges of the wall that they will not lose their seal even when the throat is at its maximum and minimum locations; the maximum movement of the throat is 0.36 centimeters and the o-rings sit at least 1.02 centimeters from the edges of the wall.

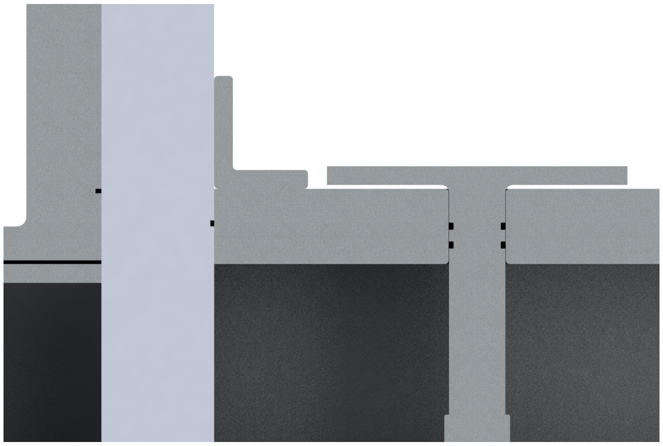

Figure 3.35: Upstream o-ring placements.

For figure 3.36, the o-rings are the small black rectangles. There are two, one sealing the box to the flange and the other sealing the flange to the test section outer wall.

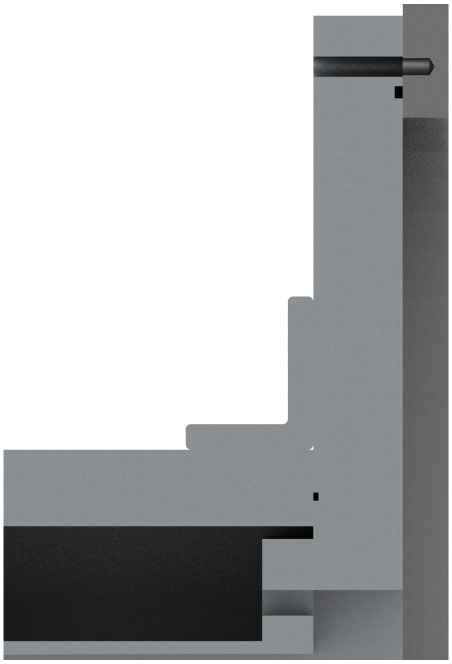

Figure 3.36: Downstream o-ring placements.

As was stated before, this design allows for variable Mach number due to changing the throat area while keeping the exit area constant. The vertical movement of the throat is caused by adding or removing shims between the jack, the T shaped piece shown in Figure 3.37, and the top and bottom walls. To hold this position, the jack is secured with 12 bolts. To know the correct height to shim the jacks to to get the desired Mach number, measurements must be taken during assembly before the attachment and welding of the fourth and final wall. Alternatively, measurements can be taken of the throat height by opening one of the side doors, but this would be more difficult than predetermining the shims due to space restrictions.

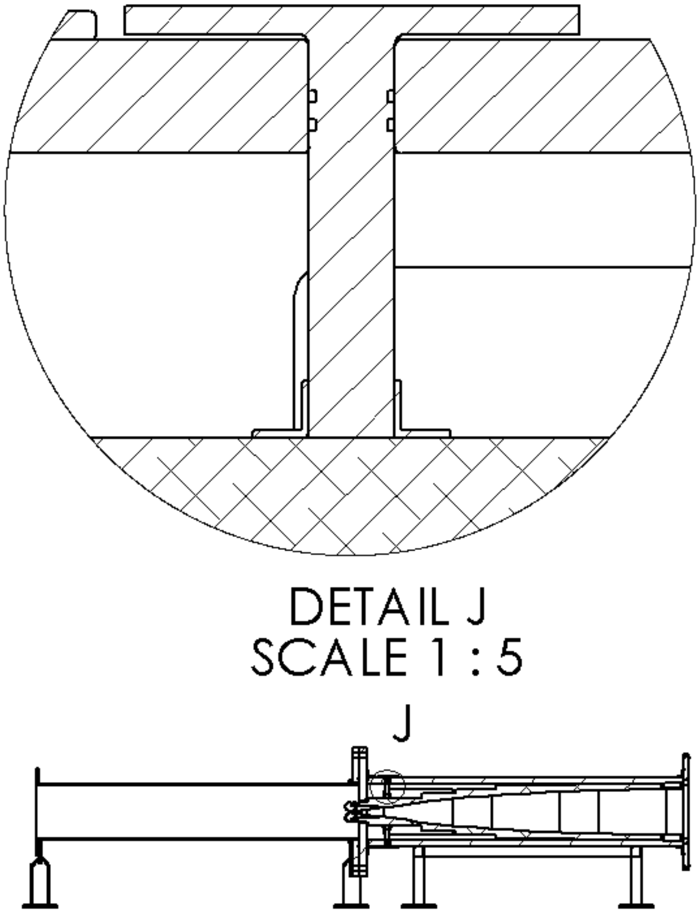

Figure 3.37: Side view of the jack.

To keep the exit area the same and to allow for the upstream movement, a flexure was designed to support the aft end of the nozzle. This is shown in Figure 3.38. There are 8 bolts on both sides connecting the flexure to the nozzle and the test section flange.

The gaps seen in the flexure on the lower right of Figure 3.38 allow for the nozzle box to be vacuumed down and pressurized with the rest of the acceleration section of the tunnel, thus reducing any leaks between the box and the nozzle itself.

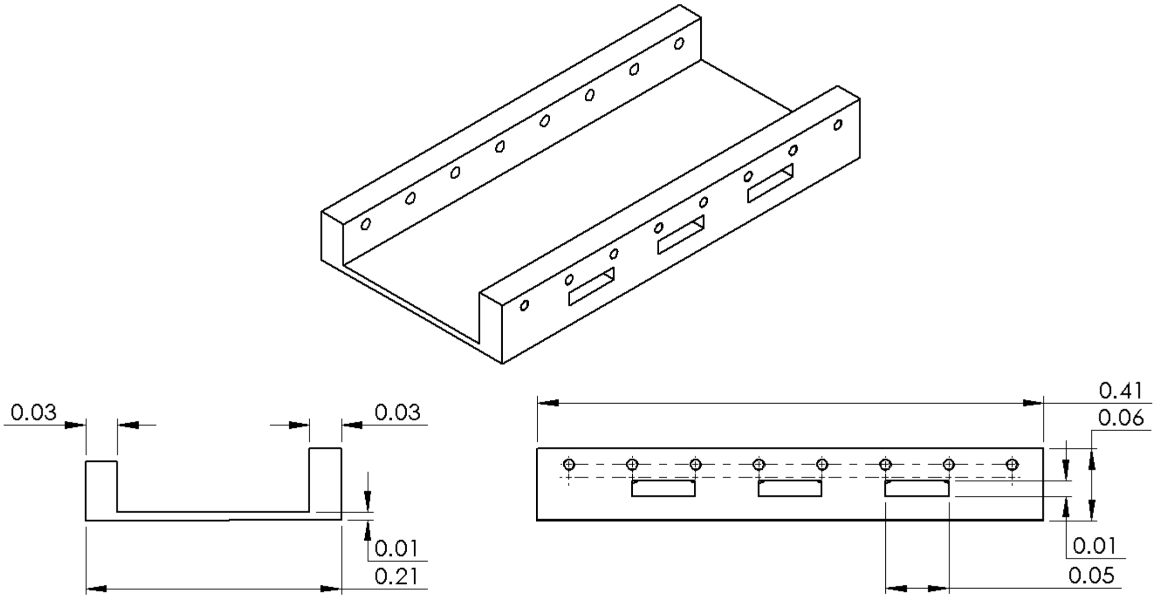

Figure 3.38: Planar nozzle flexure.

The exit of this nozzle was designed to be 16 by 16 inches or 40.64 by 40.64 centimeters, which fits within the 0.94 m diameter test section inlet. The test section flange, shown in Figure 3.39 with the flexure, is not a perfect square without the flexure due to the need to allow for the box to vacuum down through the gaps in the flexor as mentioned above and shown in Figure 3.38.

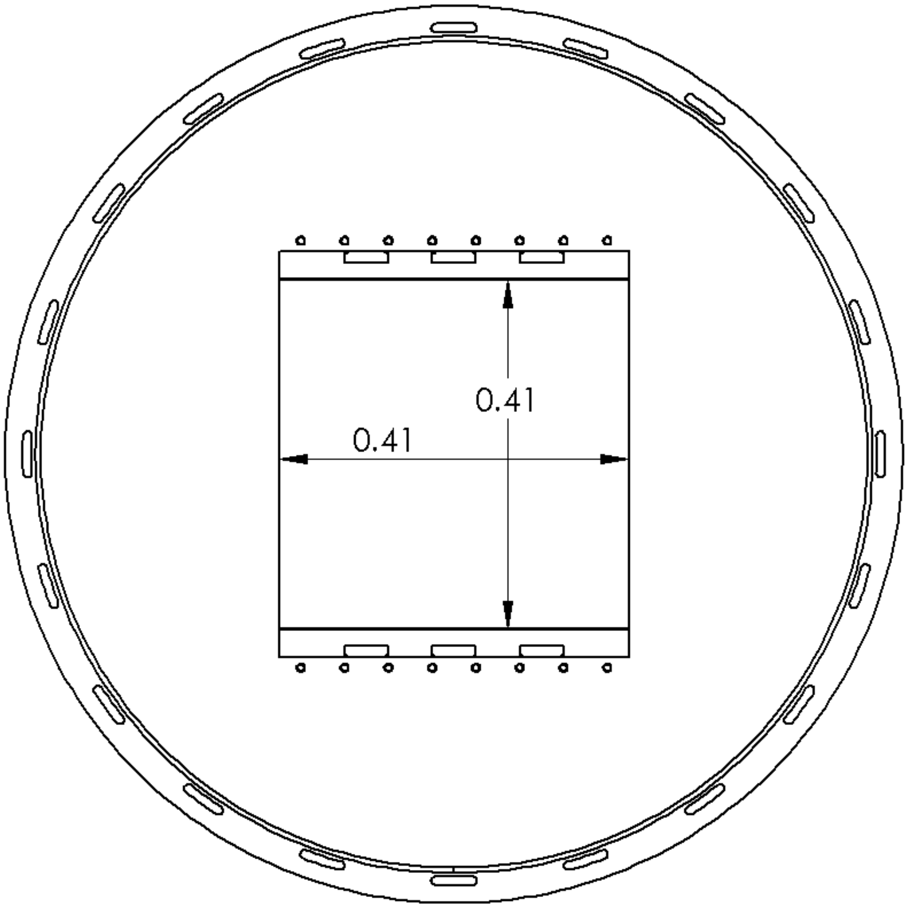

Figure 3.39: Test section flange with flexure.

Another feature of this planar design are the steps machined on the outside of the nozzle walls, shown in Figure 3.40. These steps were recommended by the engineers at the Oran W. Nicks Low Speed Wind Tunnel to help reduce the weight of the walls. This is achieved by removing material but in such a way as to be cost effective - following the inside curve of the wall on the outside as well would achieve the same thing but be more costly.

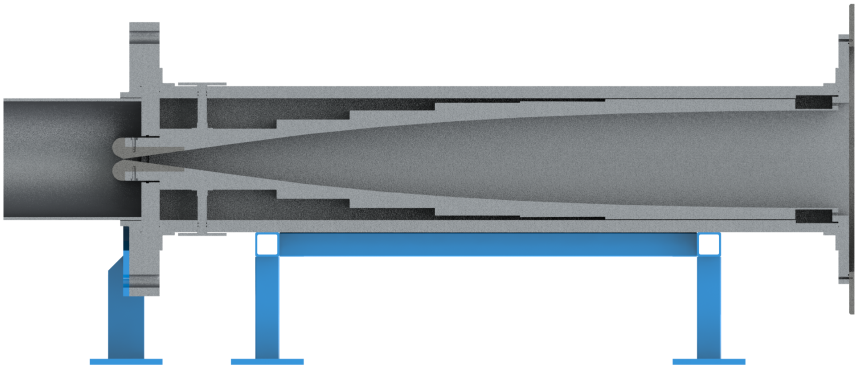

Figure 3.40: Nozzle wall steps.

3.2.3 Comparison

Overall, the planar nozzle has the most disadvantages due to the trouble of sealing the nozzle and the misaligned stand. This design is also much more complex than the axisymmetric design due to its ability to move. The current HXT nozzle is axisymmetric as well, allowing for the lessons learned from that design and manufacturing to be carried over to the design, and hopeful future manufacturing, of the new HST axisymmetric nozzle.

3.3 Heat Transfer

Three materials were tested with the code discussed in the Approach - Aluminum 6061-T6, Stainless Steel 304, and Tungsten, with their relevant properties listed below in Table 3.5. Aluminum 6061 was chosen because it is a common aluminum type and easier to machine than other types. T6 was chosen for its higher thermal conductivity over the T4 counterpart [17]. Stainless Steel 304 is what the current pipes of HXT are made out of and has a higher melting temperature compared to Aluminum [18]. Tungsten has not only an extremely high melting temperature but also has a high thermal conductivity and a high density [19], making it an excellent choice for avoiding erosion of the throat from the temperatures expected here.

Material	Density [kg/m^3]	Thermal Conductivity [W/mK]	Specific Heat [J/kgK]	Melting Temperature [K]
Aluminum 6061-T6	2,700	167.0	896	858
Stainless Steel 304	8,000	16.1	502	1,673
Tungsten	19,293	163.0	134	3,643

Table 3.5: List of material properties.

From the CFD conducted on the Mach 8 axisymmetric nozzle, the heat flux at the wall at the throat was found to be 16.7 MW/m^2. The time of interest is 30 milliseconds due to being on the same order of magnitude as the expected test time of 10 milliseconds with a factor of safety.

3.3.1 Aluminum 6061-T6

Aluminum 6061-T6, with the heat flux in the throat of the axisymmetric nozzle, takes about 362 milliseconds for the surface to reach its melting point. As was discussed earlier, this is well beyond the time expected for an actual run to take place. At 30 milliseconds, the temperature is only 456.7 K. The graph shown in Figure 3.41 illustrates the heat transfer an inch, or 2.54 centimeters, into the wall of the nozzle at the throat region at various times.

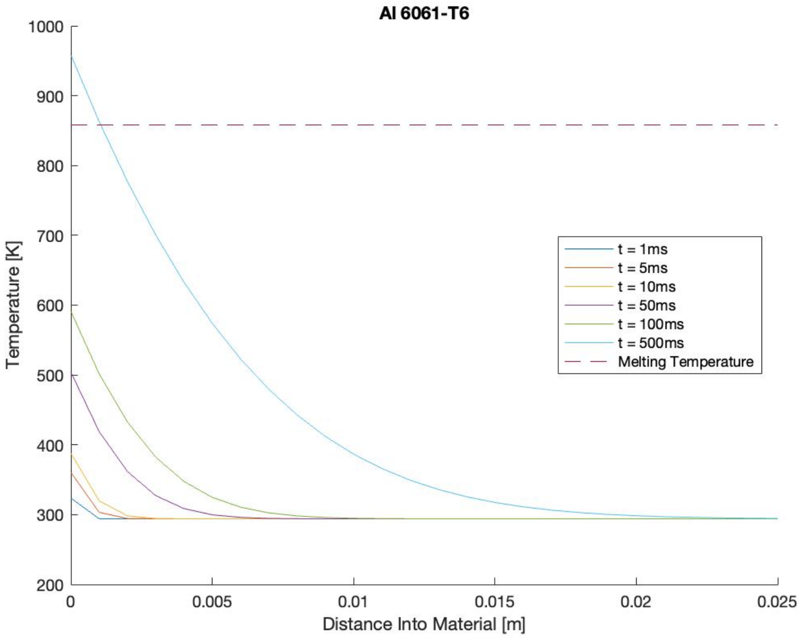

Figure 3.41: Heat transfer into an aluminum wall.

3.3.2 Stainless Steel 304

Stainless Steel 304 takes approximately 346 milliseconds for the surface to reach its melting temperature and gets to 700.8 K at the 30 millisecond mark. This is faster than the time it takes for the aluminum to reach its melting temperature by about 16 milliseconds, but is still much longer than expected run times. A similar graph to the aluminum one is shown in Figure 3.42. Steel has such a high thermal conductivity, that the heat does not penetrate very far into the wall.

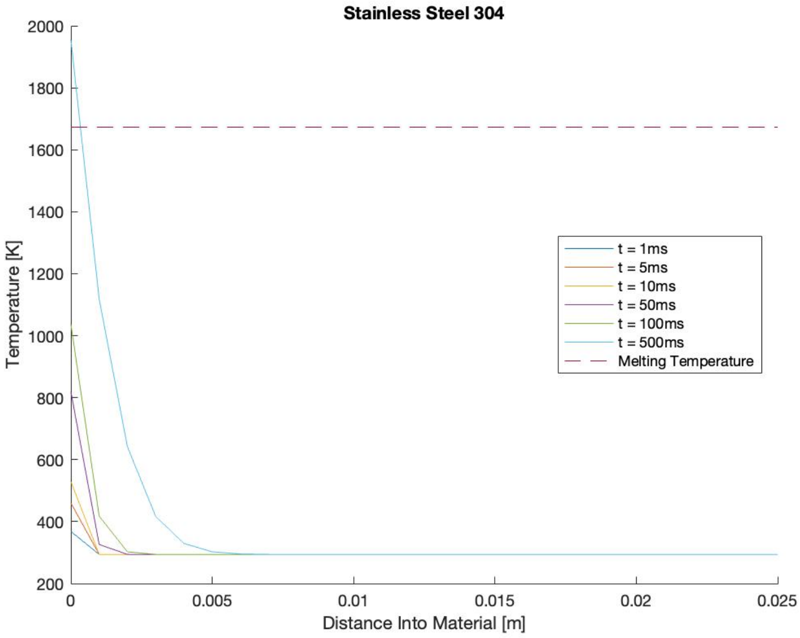

Figure 3.42: Heat transfer into a stainless steel wall.

3.3.3 Tungsten

Tungsten has the highest melting temperature of the three metals with also the highest thermal conductivity, leading to the longest time to melt yet at 13.256 seconds. To compare with the other two metals, that is 13,256 milliseconds. At the time of interest of 30 milliseconds, the surface temperature is only 453.3 K. The heat transfer graph for Tungsten can be seen below in Figure 3.43.

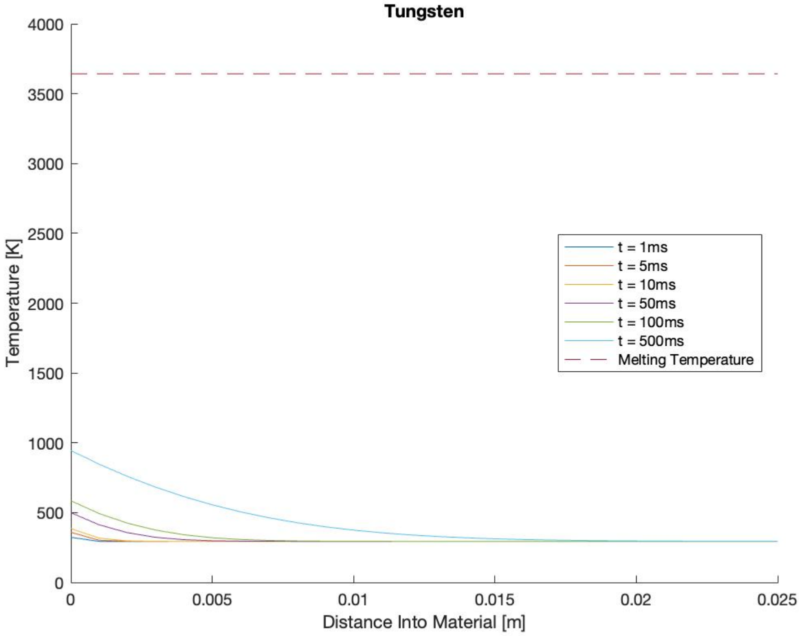

Figure 3.43: Heat transfer into a tungsten wall.

3.3.4 Comparison

The results from the heat transfer calculation are listed in Table 3.6. All three materials considered stay well beneath their melting points during the short time it takes to run the shock tunnel. However, stainless steel does get hotter at a faster rate than tungsten and aluminum, as can be seen in the past three figures and in the difference of surface temperature at 30 milliseconds (see the table below). This is due to its low thermal conductivity which is an order of magnitude below the other two (see Table 3.5). Tungsten has the largest time to melt by a wide margin compared to the other two metals, but is more expensive [19] and more difficult to machine than aluminum or stainless steel [20]. Tungsten's hardness though, makes it exceptional to resisting wear and tear from any complexities caused by the diaphragm. In the same way, stainless steel is harder than aluminum and therefore more resistant to damage, but is harder to machine because of this and generally more expensive [21].

Material	Temperature [K] at 30 [ms]	Time to Melt [ms]	Melting Temperature [K]
Aluminum 6061-T6	456.7	362	858
Stainless Steel 304	700.8	346	1,673
Tungsten	453.3	13,256	3,643

Table 3.6: Heat transfer results.

4. CONCLUSIONS AND RECOMMENDATIONS

The purpose of this work was to draw comparisons between a planar and an axisymmetric shock tunnel nozzle for the development of HST to further expand the capabilities of the facilities at the NAL.

4.1 Conclusions

CFD simulations of an axisymmetric nozzle designed for Mach 6, 8, and 10 as well as a planar Mach 6 nozzle were conducted. Detailed mechanical designs for a Mach 8 axisymmetric nozzle and a variable Mach number planar nozzle were discussed. Heat transfer at the throat of the Mach 8 axisymmetric nozzle was analyzed.

From the results discussed, the axisymmetric nozzle is a better design for HST because the exit core flow area is larger than the planar nozzle, the mechanical design is less complex, and all materials studied work well for this design.

4.2 Recommendations

For the fabrication of the converging-diverging nozzle of HST, the axisymmetric Mach 8 design is recommended. The cones should be made of 1.91 centimeter stainless steel sheets that are rolled and welded together, with the contour machined from the interior of these cones. The throat should be made of aluminum 6061-T6. Careful attention should be paid to the tolerances of this design before being sent to the manufacturer.

Real gas effects should be further studied in the axisymmetric nozzle before manufacturing to ensure performance is as expected. This can be done using a real gas model for high temperature flows or by keeping ideal gas density and changing the value of gamma. With the later, issues with convergence should be noted and accounted for by allowing for plenty of iterations and tailoring the time step the simulations take each iteration.

Investigation into the convergence problems of the planar Mach 8 and 10 nozzles should be undertaken to complete the CFD study between the two types of nozzles.

Bibliography

[1] W. Martin, “A Review of Shock Tubes and Shock Tunnels,” 1968.

[2] W. S. Stuessy, *Hypersonic Shock Tunnel Development and Calibration.* Thesis, University of Texas at Arlington, 1989.

[3] A. Dufrene, M. Sharma, and J. M. Austin, “Design and characterization of a hypervelocity expansion tube facility,” *Collection of Technical Papers - 45th AIAA Aerospace Sciences Meeting*, vol. 22, no. January, pp. 15801–15825, 2007.

[4] C. Miller, “A critical examination of expansion tunnel performance,” tech. rep., NASA Langley Research Center, 1978.

[5] H. T. Nagamatsu, R. E. Geiger, and R. E. Sheer, “Hypersonic Shock Tunnel,” *ARS Journal*, vol. 29, no. 5, pp. 332–340, 1959.

[6] J. I. Erdos, R. J. Bakos, A. Castrogiovanni, and R. Clayton Rogers, “Dual mode Shock-Expansion/Reflected-Shock tunnel,” *35th Aerospace Sciences Meeting and Exhibit*, no. January, 1997.

[7] M. Semper, N. Tichenor, R. Bowersox, R. Srinvasan, S. North, A. Texas, and C. Station, “Expansion Hypersonic Wind Tunnel,” *AIAA Paper*, no. January, pp. 1–14, 2009.

[8] M. Varner, W. Summer, and M. Davis, “A Review of Two-Dimensional Nozzle Design Techniques,” 1982.

[9] F. L. Shope, “Contour design techniques for super/hypersonic wind tunnel nozzles,” *Collection of Technical Papers - AIAA Applied Aerodynamics Conference*, vol. 4, no. June, pp. 2076–2089, 2006.

[10] K. Sabnis, H. Babinsky, D. S. Galbraith, and J. A. Benek, “Nozzle geometry-induced vortices in supersonic wind tunnels,” *AIAA Journal*, vol. 59, no. 3, pp. 1087–1098, 2021.

[11] J. Holman, *Heat Transfer.* McGraw Hill, 9 ed., 2002.

[12] R. Smelt, “Test Facilities for Ultra-High-Speed Aerodynamics,” 1955.

[13] J. Anderson, *Modern Compressible Flow with Historical Perspective*. McGraw Hill, 2012.

[14] J. Zucrow, M., Hoffman, *Gas Dynamics*. Wiley, vol 1 ed., 1976.

[15] *ANSYS FLUENT 12.0 User’s Guide*. ANSYS, INC, 12.0 ed., 2009.

[16] *Parker O-Ring Vacuum Sealing Guide*. Parker Hannifin Corporation, 50th anniv ed., 2018.

[17] “Aluminum 6061-T6; 6061-T651.” http://www.matweb.com/.

[18] “AISI Type 304 Stainless Steel.” http://www.matweb.com/.

[19] “Tungsten, W.” http://www.matweb.com/.

[20] M. Albert, “How One Job Shop Tackled Tungsten,” *Modern Machine Shop*, jun 2013.

[21] “10 Differences Between Aluminum and Stainless Steel,” 2014. https://www.metalsupermarkets.com/10-differences-aluminum-stainless-steel/.

APPENDIX A

HEAT TRANSFER MATLAB CODE

```

%Heat Transfer Calculation for Mach 8 Axisymmetric Nozzle Throat
%Written by McKenna Roberts in May 2021

clc; clear all; close all;

x = input('Choose material: Al, SS, W: ', 's');

if x == 'Al'

    k = 167; %W/mK %thermal conductivity
    Cp = 896; %J/kgK %specific heat
    rho = 2700; %kg/m^3 %density\
    alpha = k/(rho*Cp); %m^2/s %thermal diffusivity

elseif x == 'SS'

    k = 16.1; %W/mK
    Cp = 502; %J/kgK
    rho = 8000; %kg/m^3
    alpha = k/(rho*Cp); %m^2/s

elseif x == 'W'

    k = 163; %W/mK
    Cp = 134; %J/kgK
    rho = 19293; %kg/m^3
    alpha = k/(rho*Cp); %m^2/s

else
    fprintf('Error. Please input either Al, SS, or W for material.\n');
end

Q0 = 16735129; %W/m^2 %x = 0 %heat flux
Ti = 294; %K %t = 0

%Solution
T0 = @(x,t) Ti + ((2.*Q0.*sqrt((alpha.*t)./pi))./k).*exp(-(x.^2)./(4.*
    alpha.*t)) - ((Q0.*x)./k).*(1-erf(x./(2.*sqrt(alpha.*t))));
```

```

X = [0:0.001:0.0254∗1]; %0 to 1in

figure
hold on
plot(X,T0(X,0.001))
plot(X,T0(X,0.005))
plot(X,T0(X,0.01))
plot(X,T0(X,0.05))
plot(X,T0(X,0.1))
plot(X,T0(X,0.5))
xlabel('Distance Into Material [m]')
ylabel('Temperature [K]')

if x == 'Al'

    title('Al 6061–T6')

elseif x == 'SS'

    title('Stainless Steel 304')

elseif x == 'W'

    title('Tungsten')

else
end

if x == 'Al'

    T_melt = 858;

elseif x == 'SS'

    T_melt = 1673;

elseif x == 'W'

    T_melt = 3643;

else
end

Tmelt = ones(length(X),1)∗T_melt;
plot(X,Tmelt, '––')
```

```
legend('t = 1ms', 't = 5ms', 't = 10ms', 't = 50ms', 't = 100ms', 't = 500ms', 'Melting Temperature', 'location','best');

T = @(x,t) Ti + ((2.∗Q0.∗sqrt((alpha.∗t)./pi))./k).∗exp(—(x.^2)./(4.∗alpha.∗t)) — ((Q0.∗x)./k).∗(1—erf(x./(2.∗sqrt(alpha.∗t))));
t = 0.001;
TT = T(0,t);

while TT <= T_melt

    TT = T(0,t);
    t = t + 0.001;

end

MeltingTemperature = T_melt
TemperatureAtMeltingTime = TT
TimeToMelt = t
TempAt30ms = T(0,0.03)
```